Composites Science and Technology 273 (2026) 111353

Contents lists available at ScienceDirect

Composites Science and Technology

journal homepage: www.elsevier.com/locate/compscitech

Predicting the deformability of natural short-fiber reinforced polymer composites through combined constitutive mathematical and AI-based modeling approaches

N. Niang [b], T. Barriere [b], X. Gabrion [b], S. Holopainen [a,*], V. Placet [b]

[a] Tampere University, Department of Civil Engineering, FI-33014 Tampere, Finland
[b] Marie and Louis Pasteur University, SUPMICROTECH-ENSMM, CNRS, Institute FEMTO-ST, F-25000 Besancon, France

ARTICLE INFO

Keywords:
Biocomposite
Modeling & experimentation
Machine learning
Additive manufacturing (P-MEX)
Viscoelastic–thermoplastic

ABSTRACT

Biocomposites are increasingly used to reduce the use of harmful fossil plastics. Modeling and simulation tools (digital twins) have been developed to replace expensive and time-consuming physical testing during product development based on these materials. In addition to manufacturing aspects and experimentation, this study proposes a micromechanically-based constitutive mathematical model to investigate the viscoelastic–plastic deformability of biocomposites consisting of a polymer matrix and short plant fibers. Due to random fiber orientation and strong bonding between the fibers and the amorphous and crystalline phases of the polymer matrix, influence of the lattice crystalline structure was suppressed. This enables the development of a compact constitutive model. However, constitutive mathematical modeling is computationally time-consuming when applied to predict the long-term deformation behavior in large design spaces. Therefore, the proposed model is used solely to generate high-quality data for machine learning (ML) which is highly computationally efficient. The scaled-up design of new biodegradable polymeric materials, traditionally reliant on costly and time-intensive experimental procedures, is then accelerated by an advanced modeling framework that integrates constitutive mathematical models with AI-based approaches.

1. Introduction

The increasing use of fossil raw materials such as plastics has been drastically reduced by their replacement with renewable raw materials such as biocomposites including natural fiber-reinforced polymer composites [1–3]. This study introduces a set of important factors for the manufacturing, experimentation, and modeling of nonlinear (viscoplastic) deformability of natural short-fiber-reinforced (NSFR) semi-crystalline polymer composites. These composites have huge application potential because the variation in the degree of crystallization (DC) of the plastic combined with the utilization of different plant fibers (cotton, hemp, jute, flax, ramie, bagasse, conifer) and softwood can be exploited in almost unlimited range of applications such as automotive and aeronautic equipment, packaging, electronic devices, health technology, and tissue engineering [3,4].

Unfortunately, experimental studies of NSFR polymer composites are costly and time-consuming, motivating the use of predictive modeling to rapidly and systematically scan a vast number of material grades, loading conditions, and manufacturing steps. Nevertheless, research on the modeling and simulation of the mechanical behavior of NSFR polymers has been limited. Typically, the models used in previous studies have been based on very small and virtually elastic deformations [5,6]. Many models that can predict nonlinear stress versus strain (σ vs. ϵ) response are based on the assumption of nonlinear (visco)elasticity [7–11] or the response is considered to be elastic-fully plastic [12]. Previous studies have also suggested the application of the celebrated inelastic Ramberg–Osgood or Drucker–Prager models for predicting nonlinear behaviors [13,14]. Recently, [15] proposed a Perzyna-type elastic–viscoplastic constitutive model capable of predicting the overall σ vs. ϵ response of a hybrid composite (Flax/Hemp/Polypropylene, PP). However, these models do not have a clear connection to microstructural behavior, and their predictions do not represent viscous deformation behaviors such as creep, stress relaxation, and plastic residual strain (recovery at nearly zero stress).

The models particularly for fiber-reinforced polymers can be classified into mean-field and full-field models [13,16–18]. In mean-field models, the average strain and stress of a micro- or macrostructure represent the real nano- or microscopic strain and stress, respectively, and require the use of homogenization steps [19]. A notable contribution to the mean-field homogenization schemes for short fiber-reinforced

* Corresponding author.
E-mail address: sami.holopainen@tuni.fi (S. Holopainen).

https://doi.org/10.1016/j.compscitech.2025.111353
Received 25 April 2025; Received in revised form 30 July 2025; Accepted 20 August 2025
Available online 30 August 2025

composites was provided by Hessman et al. [16]. Modniks and Andersons [13] proposed a mean-field model for a short-flax-fiber-reinforced polymer where global (composite level) and local (fibers level) levels were distinguished. FEM analyses were performed on the unit cell (UC) level for parameter fitting, and finally on the composite level after homogenization. However, in addition to the complex parameter fitting, the dependence of the homogenization of the stress field on the fiber orientation affects the accuracy of the modeling. In contrast to mean-field models, full-field models account for the microscopic fields at microscopic points. These models require the use of realistic Representative Volume Elements (RVEs) that represent the microstructure of the material [9,16,18–20]. However, for high aspect ratios of fibers and high fiber volume fractions, generation of realistic and accurate RVEs can be challenging and incurs high computational costs when applied to macroscopic deformation scales.

When restricted to a sufficient fiber content, random fiber orientation, and strong bonding between the fibers and the amorphous and crystalline phases of the polymer, the influence of the complex lattice crystalline structure (with a significant anisotropy effect [21]) was suppressed. These material characteristics enabled the development of a compact constitutive model to replace most of the expensive and time-consuming experimental tests. While the set of internal variables and model parameters was reduced, the model includes the effects of the DC, fiber content, and porosity (due to voids), and therefore can reproduce dilatation-caused microstructural changes (chain disentanglement and fracture of fibril or extended chain bundles between voids [22]).

However, constitutive mathematical modeling itself is challenging and computationally time-consuming when applied to scaled-up designs and for predicting long-term deformation behavior, particularly fatigue [23,24]. Therefore, sophisticated models are increasingly being replaced by simpler and more efficient metamodels based on artificial intelligence (AI) because these models only require high-quality data [25–28]. Examples of metamodels include stochastic models and those based on statistical continuum theories. Although stochastic models have low computational costs (especially for modeling of long-term fatigue) [29–31], they have not been widely used due to their limited convergence, particularly for high-contrast composites [29].

Recently, data-driven modeling approaches based on ML (a remarkable subset of AI) have shown promise for simulating nonlinear deformation behavior of biocomposites [17,32]. Thomas and Barocio [33] predicted the mechanical properties of fiber-reinforced composites using ML algorithms (the so-called deep material networks, DMN), and found that the amount of the required experimental efforts can be reduced by using ML. Yang et al. [25] investigated deep-ML approaches for mining structure–property relationships in high-contrast elastic composites from artificial datasets predicted by the neural networks models. Laycock et al. [27] proposed the Materials 4.0 concept which refers to the present digital materials revolution by combining ML (4.0) with experimental (1.0), theoretical (2.0), and computational (3.0) materials science knowledge. Recently, Ling et al. [31] proposed a ML method to predict the macroscopic stress–strain relationships of thermoplastic polymers using the Kriging (stochastic) ML model, a genetic algorithm (GA) for training the ML model, and limited experimental testing data. However, the shortcoming in those previous works is that they presume costly experimental data and ignore the optimal relationship between the experimental data (partially missing due to costs) and the predicted model data (unlimitedly available).

The present work combines the benefits of traditional mathematical modeling and AI-based modeling, with the experimental data typically used for ML training replaced by predicted high-quality model data. Model predictions or simulated data are of particular interest for replacing expensive experimental data, with the value of these data predicted to grow exponentially in the future [34,35]. Moreover, the proposed modeling framework, which couples constitutive mathematical modeling with AI-based techniques, enables a huge reduction of calculation times, particularly when applied to predict long-term deformation behaviors. It is emphasized here that fundamentally different from the previous works, the predicted model data provide experimentally-supported data for ML training while understanding the theoretical microstructural properties and performance of biocomposites. The concept of using ML based on advanced physical (micromechanically based) modeling is illustrated in Fig. 1.

2. Methods

2.1. Manufacturing

A semi-crystalline polylactic acid (PLA) polymer and its composites reinforced with natural short hemp fibers were used as the case study, resulting in notably viscous (elastic–plastic) deformability. PLA (type PLI 005 supplied by Natureplast) was used because it is one of the most widely globally used polymer matrices (with production capacity of approximately 211,000 tons in 2020 [36]) in biocomposites (notably high Global Warming Potential, GWP) which are used to replace non-renewable petroleum-based materials [37,38]. The PLA polymer is also widely used for filaments and biodegradable waste in 3D printing [27, 39]. PLA is a biodegradable polyester that is typically obtained from sustainable agricultural waste such as maize, potatoes, and cassava through bacterial fermentation of carbohydrates.

Hemp fiber was selected because it is obtained from an abundant European fiber plant and offers numerous ecological and economic advantages. The global market value of hemp-based products is USD ~2 billion and is growing rapidly [40]. Additionally, hemp shows good compatibility with PLA, enhancing the flexural, tensile, and impact properties of this polymer [37,41–43]. Hemp has a higher cellulose content (~ 70 %wt) than softwood (~ 40 %wt), which is an important property, because cellulose maximizes the stiffness and strength of a material, whereas lignin of the softwood decreases strength (although it may improve ductility) [44]. Short fibers (~ 160 μm) were used because of their beneficial effects on the tensile strength. The fibers were obtained through hammer milling and a defibration process that extracts the fibers from the stalk via several mechanical operations, culminating in mechanical cleaning of the fibers. A well-homogenized mixing of the matrix and fibers was achieved using a twin-screw extruder dedicated to the production of biocomposite mixtures at 30 rpm and 190 °C, as shown in Fig. 2(A–B).

The goal of this study is to develop biodegradable composites which are also highly malleable (plastically deformable) near room temperature (RT) under the abovementioned material constraints (PLA + hemp). Such composites enable reduced energy consumption and less expensive machining [45] (particularly important for cold forming). The following important observations regarding the increased plastic deformability (ductility) were obtained during the experiment:

1. the increased deformability is strongly influenced by the content and type of plasticizer,
2. the deformability decreases with lower porosity,
3. the deformability decreases with higher hemp content.

Notably, PLA exhibits limitations in the deformability near RT [46]. The polyethylene glycol (PEG) additive (plasticizer) with a molecular weight of 1.5k and 20k (5%wt) was used to increase the deformability (plasticity) of the composite, see the details in Fig. 3. In addition, PEG 400, 600, 1k, and stearic acid (SA) were applied but achieved lower performance. Second, when the porosity of the composite was reduced from 8%–9% to 4%, the deformability as measured by the strain decreased from 3% to 1%, indicating an elastic response. The third observation is in line with previous observations [47]; that is, the gains obtained by replacing the polymers with the biomaterial (hemp) are counterbalanced by the decrease in the ductility of the composite. However, the tensile strength of the pure matrix can be improved by bio(hemp) fibers [37,41–43].

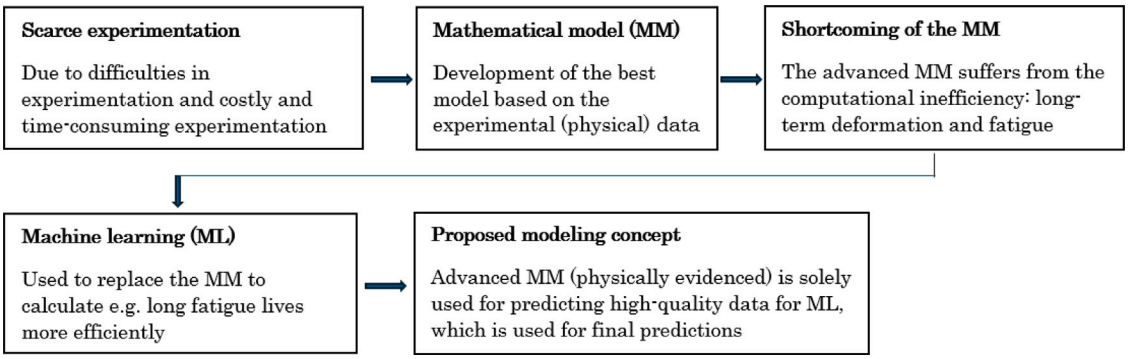

Fig. 1. Flowchart for ML modeling based on experimental data and the high-quality data predicted by the advanced physical model (based on available experimental data).

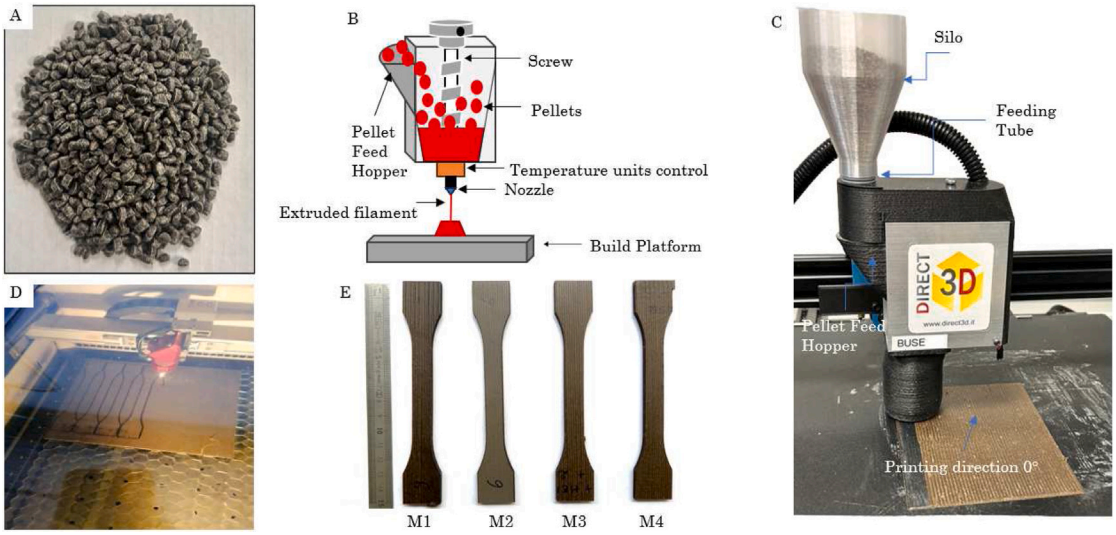

Fig. 2. Manufacturing of the tensile test specimens: PLA–hemp pellets (A), details of the 3D printing with the P-MEX (B), printing of the plate (C), laser cutting of the test specimens (D), and final dogbone-shaped specimens (following the standard ISO 527–4 type 1B specimen) (E).

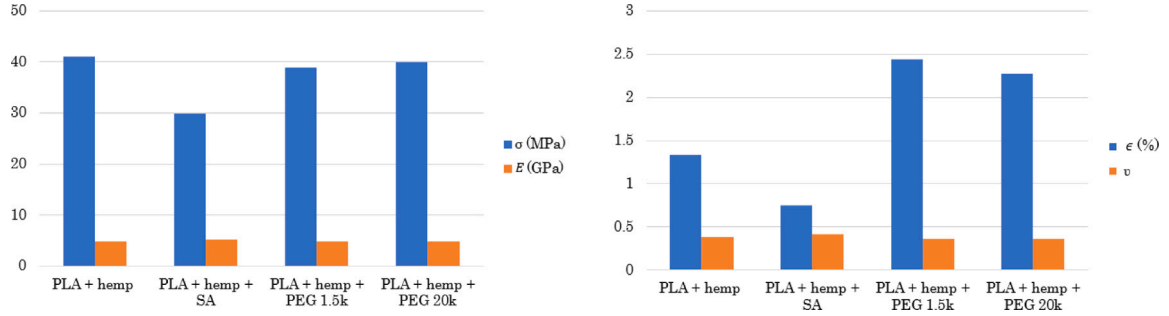

Fig. 3. Pure PLA-hemp and the influence of additives (5%wt) on its tensile properties (the Young's modulus E, ultimate strength σ and strain ϵ, and the Poisson ratio υ) at the printing direction. The hemp fiber content was 20%wt.

Dogbone-shaped tensile specimens were manufactured via 3D-printing using pellet-based material extrusion (P-MEX) [38] in accordance with the ISO 527–4 standard (type 1B specimen), as shown in Fig. 2(C–E). 3D-printing with P-MEX is advantageous in that it uses pellets directly, without the need to manufacture a homogeneous calibrated (wound or unwound) filament to withstand the shear and buckling associated with controlling the filament feed into the molten polymer extrusion zone. The 3D-printer with the pellet extruder was compatible with the standard *.gcode files generated by the most popular slicing software (e.g. Slic3R, Repetier, Cura, Simplify3D, IdeaMaker).

Overall, the structure and properties of a biocomposite are the result of a complex interplay between the fiber content, fiber–matrix adhesion, fiber dimensions, matrix porosity, DC of the matrix, printing conditions (e.g. nozzle temperature, printing speed, layer thickness), environmental conditions (temperature and humidity), and the manufacturing facilities [37,38,42].

It was observed that high fiber content, high layer thickness, high printing speed, and low nozzle temperature tended to increase the porosity and decrease the deformability of the composite. The optimal nozzle temperature, layer thickness, and printing speed were found to be 190 °C, 0.4 mm, and 40 mm/s, respectively. Moreover, the pellets

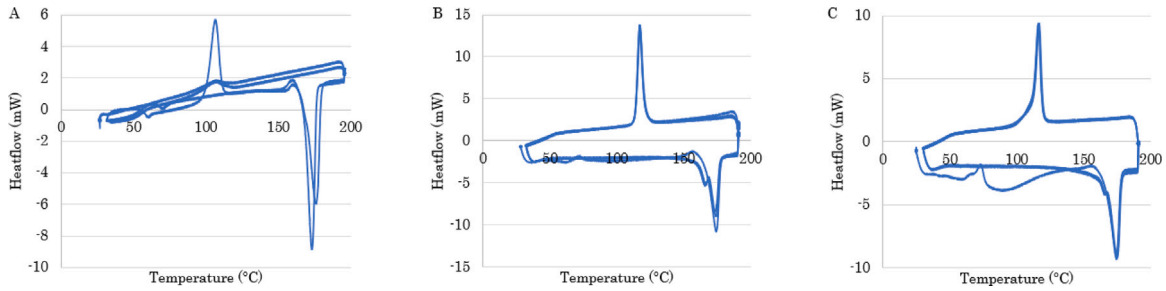

Fig. 4. DSC plots for the PLA matrix (A), the composite (PLA + hemp + PEG 20k) before printing (B), and the composite after printing (C). The hemp fiber and plasticizer contents were 20%wt and 5%wt.

were dried prior to printing at 60 °C for 3 h. A hemp fiber content of 20%wt in the PLA (significantly higher fiber content compared to most plastic biocomposites [48]) was found to be optimal for obtaining high-quality extrusion and surface finish by the printer. An overall review of 3D-printing manufacturing is presented in Duigou et al. [49], Ilyas et al. [37], Proy et al. [50], Nazir et al. [38]. The most important conclusion regarding material development and production (printing) is that the transition from brittle elastic deformation of the material to ductile plastic is a sensitive process and can be achieved by using the optimal fiber content, porosity, and a plasticizer. The optimal composite was PLA + hemp (20%wt) + PEG 20k (5%wt) with a porosity of 8%–9%.

2.2. Experimentation

Crystallinity

The DC values of the matrix and composite were revealed by differential scanning calorimetry (DSC; Setaram Equipment DSC 131 EVO in air atmosphere). For each measurement, a sample (30 mg) was placed in aluminium, and the crucible was crimped and sealed hermetically. The sample was then heated at a rate of 3 °C/min from 25 °C to 195 °C and maintained in the molten state for 10 min in order to erase the previous thermal history. It was then cooled at the same rate to 25 °C, allowing the evaluation of its hot crystallization. Subsequently, the sample was reheated to 195 °C at a rate of 3 °C/min to evaluate the cold crystallization. During heating, the first significant exothermic peak (A) was observed due to crystallization, cf. Fig. 4. Then, another endothermic peak (B) appeared that is attributed to the melting of the crystalline polymer fraction. The DC was calculated as $DC = \Delta H_f / \%PLA \cdot \Delta H_{f0}$, where ΔH_f, $\%PLA$, and ΔH_{f0} are the measured enthalpy of fusion (~ 42 J/g), matrix content (PLA), and hypothetical enthalpy of fusion of 100% crystallinity (93 J/g for PLA). The DC of the composite was observed to be 38% when the fiber content was 20%wt, and the DC of PLA was 52%; that is, the composite and PLA matrix were semi-crystalline, and the DC of the composite was controlled by the fiber content.

Porosity

A high-resolution Solution X-ray tomography system with a 150 kV X-ray generator (Solution Easytom) was used to determine the porosity, fiber orientation, and fiber content of the composite. The tomography system can acquire 1440 images per min through 360 ° (in the fly mode), resulting in a total tomography time of 30 min. Data processing for the detection of the porosity zones was performed using the VG STUDIOMAX 2023 software, and the segmentation of porosity was performed with a threshold based on the gray level. The grayscale in the acquired computed tomograph (CT) images corresponds to X-ray absorption, with darker levels indicating lower X-ray transmission (i.e. porosity, see, for example, Fig. 5(right)). The CT images revealed pore size, shape, and distribution, which are crucial for material quality and mechanical properties. However, this method has drawbacks including reliance on costly equipment and expertise, as well as adjustment of resolution and contrast. Scanning electron microscopy (SEM) was also used to observe the porosity, as shown in Fig. 5(bottom left).

In contrast to the experimental methods, direct porosity calculation methods such as weight-based approaches are simple and cost-effective (although they are limited by material property assumptions that have limited accuracy). Therefore, in addition to the CT scan porosity, the average porosity (%) of the composite was directly calculated according to $(1 - P_{wt}/T_{wt})100\%$, where P_{wt} and T_{wt} are the weights of the printed sample, and the theoretical weight is calculated as the product of the measured volume and theoretical density (%wt-weighted combination of the matrix, fiber, and plasticizer). The porosity of the composite with the PEG plasticizers was found to be between 7%–9% , as shown in Fig. 5(top left). It was observed that the plasticizers had no marked influence on the rate of porosity development; however, due to use of plasticizers, porosity became much more localized and the plasticizers reduced the volume of intrabead voids.

Deformation

The uniaxial tensile tests at RT (isothermal conditions) were performed using an MTS Criterion Model 45 machine equipped with a 5 kN load cell. Prior to testing, the material was held at RT (50%RH) for 14 days for stabilization. Tests were conducted at least twice to ensure reliability. The test set was designed to determine the Young's modulus, tensile strength and the corresponding strain at failure, and to observe the nonlinear shape of the stress–strain curve, see Fig. 6(left). The monotonic loading was displacement-controlled, which means that it was regulated by the movement speed of the top plate, as illustrated in Fig. 6(right). A strain rate $\dot{\epsilon} = 2$ mm/min$/L \sim 0.001/s$ was applied and an extensometer with a gauge length $L = 25$ mm was used to measure the axial elongation u. The corresponding axial strain is $\epsilon = u/L$, and the stress was calculated as $\sigma = F/A$, where F is the applied force and A is the initial cross-sectional area of the gauge section of the specimen. Such 1st Piola–Kirchhoff stress and engineering strain can be easily measured and were used in the modeling. The relationship between the $\boldsymbol{\sigma}$ (components (i, I)) and the Kirchhoff stress $\boldsymbol{\tau}$ is given by $\Sigma_{j=1}^{3} \boldsymbol{\tau}(i,j)\boldsymbol{F}^{-1}(I,j)$. It can be concluded that the difference between the stress measures is small when the strain is restricted (less than 10%) [51].

Anisotropy

Fig. 7(left) shows a bimodal distribution of the fiber orientation, with a large majority of the fibers oriented in the $0 - 40^o$ range (with the distribution peak at approximately 20^o) and a significant portion oriented transversely (approximately $80-90^o$). This distribution is notable even when compared to the orientation distribution for anisotropic composites [52]. It was also observed that the reductions in the tensile strength and the elastic stiffness (in terms of the Young's modulus) were relatively small, ~ 20 %, when the loading direction was changed from 0^o to 90^o relative to the printing direction. Moreover, Fig. 7(right) shows that the Poisson's ratio of the composite varies between 0.34–0.44 and 0.32–0.40 during deformation when the loading

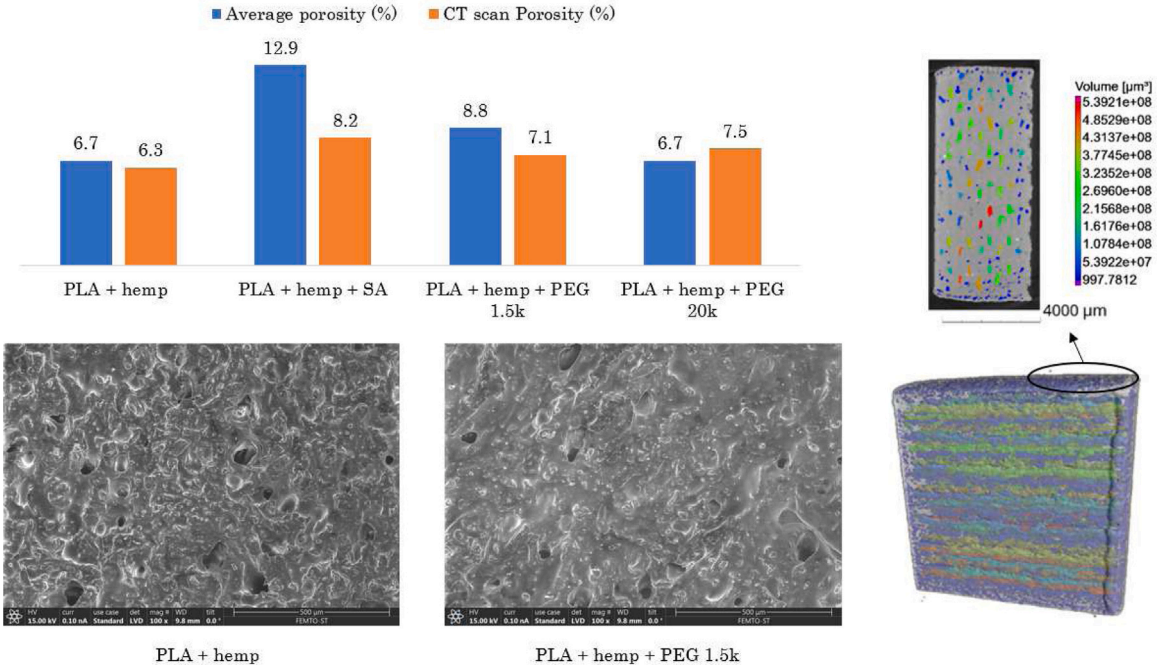

Fig. 5. Porosity of printed specimens (top left) and SEM images for porosity (black regions) without and with added 5%wt of PEG 1.5k plasticizer, respectively (bottom left). Corresponding CT scan (with the addition of 5%wt of PEG 1.5k) for the porosity (right).

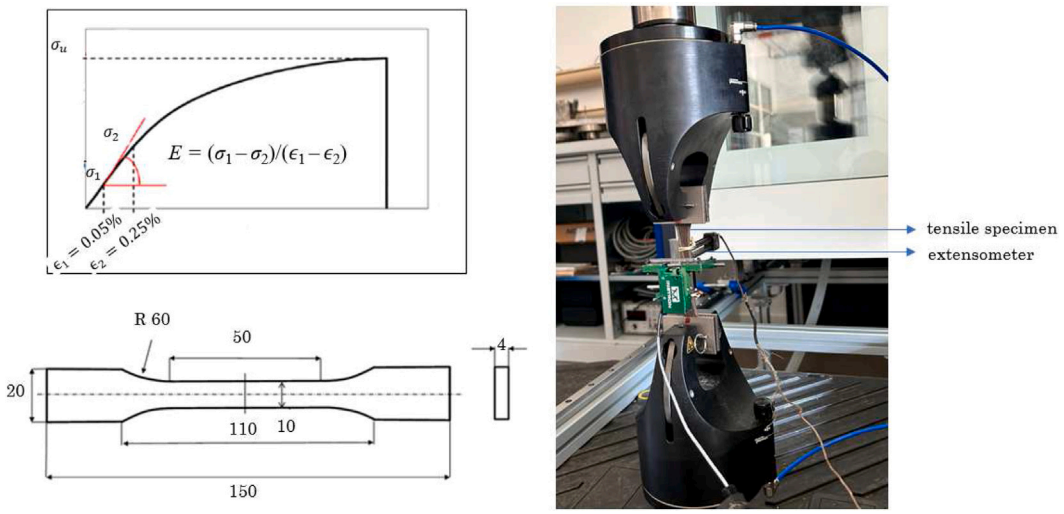

Fig. 6. Definition of the deformation measures (incl. the Young's modulus, E, and the tensile strength, σ_u) and dimensions of the test specimen (left). The tensile test setup (following the standard ISO 178) including the extensometer (right).

is carried out in the 0° and 90° directions, respectively. The observed differences of ~ 10 % in the Poisson's ratio are relatively small, and the average Poisson's ratio $\nu = 0.37$ typical for solid PLA reported in the literature is applicable. Based on the observed results, the composite can be considered to be macroscopically almost isotropic.

Nomenclature

$\boldsymbol{F}$, $\boldsymbol{F}^{\mathrm{vep}}$, $\boldsymbol{F}^{\mathrm{e}}$	deformation gradient and its viscoelastic–plastic and elastic components
$\boldsymbol{F}^{\mathrm{f}}$, $\boldsymbol{F}^{\mathrm{a}}$, $\boldsymbol{F}^{\mathrm{c}}$	deformation gradient of the fiber, amorphous, and crystalline components
ϵ	uniaxial strain ($= \ln(\sqrt{\boldsymbol{F}\boldsymbol{F}^{\mathrm{T}}})$)
$\boldsymbol{\sigma}$, $\boldsymbol{\sigma}^{\mathrm{f}}$, $\boldsymbol{\sigma}^{\mathrm{a}}$, $\boldsymbol{\sigma}^{\mathrm{c}}$	macroscopic stress and its fiber, amorphous, and crystalline components
υ, υ^{f}, υ^{a}, υ^{c}	Poisson's ratios of the composite, fiber, and amorphous and crystalline phases
E^{f}, E^{a}, E^{c}	Young's moduli of the fiber, amorphous, and crystalline phases
E, E_{m}	Young's moduli of the composite and its matrix
ζ, χ, ξ	porosity, DC, and fiber content
$\bar{\boldsymbol{L}}^{\mathrm{vep}}$, $\bar{\boldsymbol{D}}^{\mathrm{vep}}$	viscoelastic–plastic velocity gradient and its symmetric component
η	viscosity
$\dot{\gamma}^{\mathrm{vep}}$	viscoelastic–plastic shear strain rate
τ, s^{a}	effective stress and shear resistance to plastic flow
$\dot{\gamma}_0^{\mathrm{a}}$, m, ς	model parameters

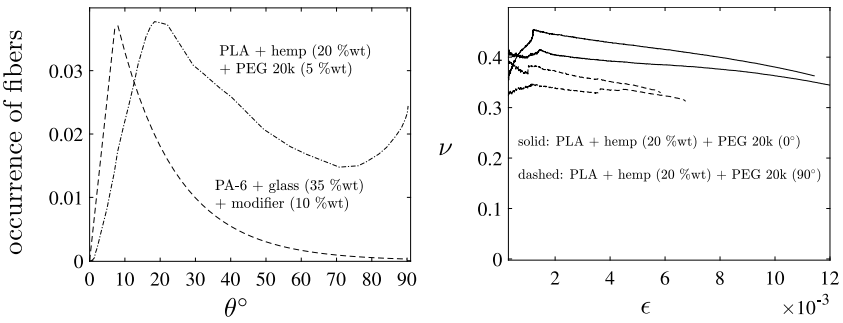

Fig. 7. Fiber orientation (relative to the printing direction 0 °) vs. fibers volume fraction based on CT (left). The fiber orientation of an anisotropic composite (dashed curve) is taken from Mortazavian and Fatemi [52]. Measured in-plane Poisson's ratios of the composite (with the addition of 5%wt of PEG) in the two main directions (right). Each experiments was conducted twice. Another extensometer was used to measure the transverse deformation.

3. Modeling

3.1. Fibers vs. matrix

The following assumption were made: [1] short fibers (average fiber length ∼ 160 μm) are homogeneously and random distributed, [2] strong bonding between fibers and the matrix, [3] no significant content of (intra-bead) voids, that is, low porosity (<10%), and [4] a sufficiently high content of (elastic) fibers, $\xi \geq 20$ %wt. Moreover, the polymer matrix and its biocomposite including plant fibers are considered to be semi-crystalline; that is, the DC is greater than 10% [21]. Influence of the fiber aspect ratio relative to the void volume and fiber content was considered to be weak because a short fiber length (although with a sufficiently high aspect ratio without a shape effect [5]) has been demonstrated to have only a limited effect on the predicted composite properties [5,13]. The first assumption ensures a uniform distribution of the fibers without marked anisotropy; the second assumption prevents sliding between the fibers and the matrix; the third assumption ensures a sufficiently uniform microstructure without marked porosity; and the fourth assumption ensures that fiber deformation governs the total deformation of the material, particularly the elastic deformation. As the fibers were short and randomly distributed, the initial elastic response was homogeneous and essentially isotropic, and no homogenization of the stress based on the fiber orientation was required. This can be verified using the Voigt average stress in a misaligned fiber composite under an applied strain given by

$$\sigma_{ij}(\epsilon) = \frac{1}{4\pi}\int_0^{2\pi}\int_0^{\pi} {\sigma^{UD}}_{ij}(\epsilon,\varphi,\theta) f(\varphi,\theta)\sin(\theta) d\varphi d\theta, \tag{1}$$

where ${\sigma^{UD}}_{ij}$ stands for the stress under a given applied strain in a unidirectionally aligned (UD) fiber-reinforced computational element of the composite and $f(\varphi,\theta)$ denotes the fiber orientation distribution density as a function of the azimuthal, φ, and elevation, θ, angles [5,13]. When the fibers are randomly arranged, $f(\varphi,\theta) = 1$ and ${\sigma^{UD}}_{ij}(\epsilon) = \sigma_{ij}(\epsilon)$.

To enable investigations of composites showing notable plasticity, the model is based on the decomposition of the deformation gradient (at position $\boldsymbol{X}$ and time t) into the elastic and viscoelastic–plastic contribution, that is,

$$\boldsymbol{F} = \boldsymbol{F}^{e}\boldsymbol{F}^{vep}, \quad J = \det(\boldsymbol{F}) > 0, \quad \boldsymbol{F}(\boldsymbol{X}, t=0) = \boldsymbol{1}, \tag{2}$$

where $\boldsymbol{F}^{e}$ and $\boldsymbol{F}^{vep}$ determine the local deformations resulting from elastic and viscoelastic–plastic mechanisms, respectively [53]. Fig. 8(left) illustrates the microstructural deformation behavior of NSFR semi-crystalline polymers. The deformation of plant fibers (hemp) is limited, and they are often considered to be practically elastic [13], whereas the polymer matrix governs viscoelasticity (reversible deformation in time) and viscoplasticity (irreversible deformation). When DC is sufficiently low (less than 50%), the deformation of the crystalline phase relative to the amorphous phase is small [54] (Fig. 2), and it can be assumed to be elastic without a significant error in the total deformation. Furthermore, due to the very high strength and limited (elastic) deformability of the fibers relative to the matrix (both crystalline and amorphous phases) and strong bonding between the matrix and fibers (including sufficiently high fiber content), the crystalline phase and the elastic portion of the amorphous phase deform on average (microstructurally) in accordance with the fibers; the applied fiber length is on the order of 100 μm (here, 160 μm on average for hemp) which is several orders of magnitude longer than the amorphous chain lengths and dimension of the crystalline regions (on the order of 100 nm) [55]. Subsequently, the elastic deformation of the matrix is controlled by the elastic deformation of the fibers and the compatibility condition $\boldsymbol{F}^{e,a} = \boldsymbol{F}^{c} = \boldsymbol{F}^{f} = \boldsymbol{F}^{e}$ (a=amorphous, c=crystalline, f= fiber) for the elastic deformation is applicable.

The rheology of the model is illustrated in Fig. 8. The proposed model is the three-dimensional extension of the celebrated Maxwell (1867) model, which is known to be capable of capturing stress relaxation. In addition, the proposed model can predict nonlinear unloading and long-term creep under relatively low stress levels (slow creep accumulation), which is important for practical applications.

The average macroscopic stress in the fibers is given by

$$\boldsymbol{\sigma}^{f} = \xi\mathfrak{L}^{e,f} : \ln\boldsymbol{v}^{e} = \xi E^{f}/(1+\nu^{f})\ln\boldsymbol{v}^{e} + \xi E^{f}/[3(1-2\nu^{f})]\mathrm{tr}\,(\ln\boldsymbol{v}^{e})\boldsymbol{i}, \tag{3}$$

where ξ is the fiber content (%wt), E^{f} is the Young's modulus, ν^{f} is the Poisson's ratio, the notation tr denotes the tensor trace, and $\boldsymbol{v}^{f} = \boldsymbol{v}^{e} = \sqrt{\boldsymbol{F}^{e}\boldsymbol{F}^{e,T}}$ is the elastic stretch tensor described in Belytschko et al. [51], Holopainen and Barriere [56]. When the fiber content is infinitesimal, its stress effect in the composite vanishes. If the fibers after printing display a significant orientation (Young's moduli and Poisson's ratios show differences of more than 20% between the printing direction and transverse direction [52]), it is necessary to replace the elastic stiffness tensor $\mathfrak{L}^{e,f}$ in (3) by the orthotropic (transversally isotropic) tensor [51].

3.2. Crystalline phase

Due to the sufficiently high fiber content and strong bonding between the fibers and the amorphous and crystalline phases of the semi-crystalline polymer, the influence of the classical slip systems of crystal plasticity, including the inherent lattice structure [21] is suppressed. For NSFR semi-crystalline polymers with a random distribution of fibers, there are no preferred directions of crystallites other than the principal directions of stress because compared to the influence of amorphous chain and fiber orientation, the influence of crystallinity is small. Furthermore, when DC was sufficiently low (less than 50%), the deformation of the crystalline phase relative to that of the amorphous phase was small, cf. Bartczak [54] (Fig. 2), as demonstrated in Fig. 8(left). Therefore, many models based on fiber orientation [17] and the so-called layered two-phase composite inclusion (TPI) [21] for semi-crystalline polymer matrix can be significantly simplified. That

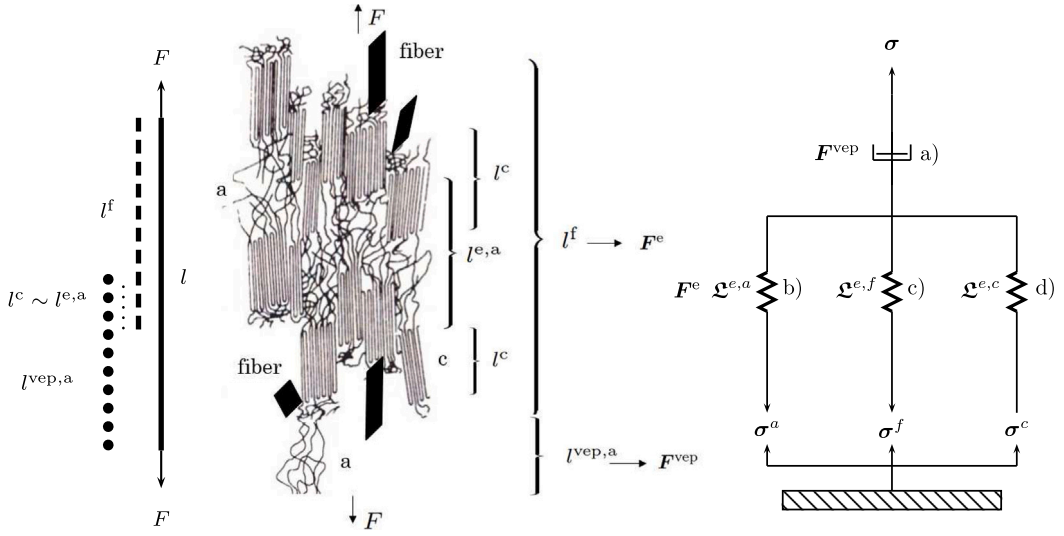

Fig. 8. Demonstration of the deformed microstructure of the NSFR semi-crystalline polymer driven by the force F (left). The solid thick bar demonstrates the total deformation (current length, l), dashed thick bar is the fiber deformation (current length, l^f), dotted thick bar is the (amorphous, a) viscoelastic–plastic deformation ($l^{vep,a}$), and the vertical stroke (dotted) means the deformation of the crystalline and amorphous elastic phases ($l^c \sim l^{e,a}$, not equal, but small in relation to fiber and amorphous viscoelastic–plastic deformation). Rheological representation of the microstructure-based model (right): the current length $l^{vep,a}$ of an amorphous phase is described by $\boldsymbol{F}^{vep}$ and a single nonlinear viscoelastic–plastic dashpot (a), and the current length of the elastic amorphous phase $l^{e,a}$, the fiber l^f (elastic), and the crystalline phase l^c (∼ elastic) are described by the elastic springs (b), (c), and (d), respectively.

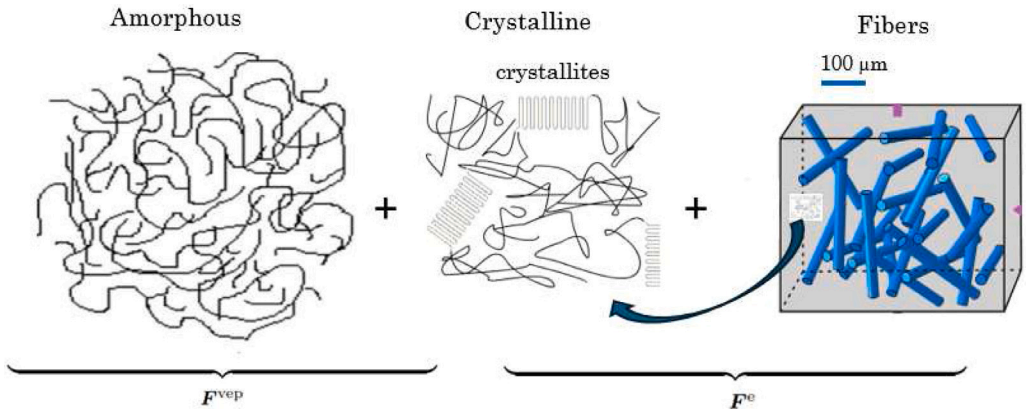

Fig. 9. Concept of the model: the total deformation is due to the joint effects of randomly distributed (amorphous) polymer chains (viscoelastic–plastic, $\boldsymbol{F}^{vep}$) (left), crystalline regions of the matrix (middle), and short fibers (right). Fibers and crystalline regions deform essentially elastically ($\boldsymbol{F}^e$). Orientation of the fibers during printing may give rise to anisotropy.

is, without inducing a significant error in the total deformation, the deformation of the crystalline phase can be considered small and elastic, particularly when the deformation of the entire composite is sufficiently small, that is, less than 10% (see Fig. 9).

The crystalline phase also exhibits anisotropy due to the alignment of the crystalline regions [21]. However, inspection of NSFR polymers at the micro- to macro-level shows that crystalline regions are randomly arranged, and the effect of their anisotropy relative to that of the fibers is small (the dimensions of fibers of ∼ 160 μm are much greater than those of crystalline regions of ∼ 100 nm). Overall, the kinematic compatibility condition $\boldsymbol{F}^e = \boldsymbol{F}^f = \boldsymbol{F}^c$ prevails and the average macroscopic stress over the crystalline regions is given by:

$$\boldsymbol{\sigma}^c = (1-\xi)\mathfrak{L}^{e,c} : \ln \boldsymbol{v}^e = (1-\xi)E^c/(1+\nu^c)\ln \boldsymbol{v}^e + (1-\xi)E^c/[3(1-2\nu^c)]\mathrm{tr}(\ln \boldsymbol{v}^e)\boldsymbol{i}, \tag{4}$$

where ν^c is the Poisson's ratio of the crystalline regions and E^c is the corresponding Young's modulus with the relations [a] $(1-\zeta)E^m = \chi E^c + (1-\chi)(1-\zeta)E^a$ and [b] $E = \xi E^f + (1-\xi)(1-\zeta)E^m$ (along with the prerequisites [1-4]), where $\zeta < 0.1$, $0.1 < \chi \leq 0.5$, $\xi > 0.2$, E^m, E^a, and E^f are the porosity, DC, fiber content, and the Young's moduli of the matrix, its amorphous phase, and the fibers, respectively. Therefore, it is necessary to measure solely the Young's moduli of the composite, matrix, and its amorphous phase, whereas E^c and E^f are calculated from relations [a] and [b]. E^f can be termed the functional fiber stiffness (average modulus for the three main directions [57]) of the composite. Most importantly, the elastic deformation strongly depends on the porosity, DC, and fiber content; in particular, the elastic deformability increases with porosity and decreases with fiber content (through the Young's modulus). This statement is consistent with the observations that the plastic deformability (ductility) decreases with lower porosity and higher fiber content, cf. the list 1. - 3. in Section 2.1.

3.3. Amorphous phase

Amorphous polymers are known to exhibit viscoelastic–plastic deformation immediately upon loading [23,53,58]. Therefore, the amorphous phase in the composite is considered to be viscoelastic–plastic and undergoes the total viscoelastic–plastic deformation, that is $\boldsymbol{F}^{vep} =$

$\boldsymbol{F}^{\mathrm{vep,a}}$. The viscoelastic–plastic component $\boldsymbol{F}^{\mathrm{vep}}$ in (2) is manifested as macroscopic nonlinear monotonic loading, long-term creep strain, stress relaxation, and nonlinear unloading response due to the inertia of the nano-microstructure in attaining equilibrium, and is calculated as

$$\dot{\boldsymbol{F}}^{\mathrm{vep}} = \bar{\boldsymbol{L}}^{\mathrm{vep}} \boldsymbol{F}^{\mathrm{vep}}, \tag{5}$$

where $\bar{\boldsymbol{L}}^{\mathrm{vep}}$ is the velocity gradient defined below.

According to this model, the viscoelastic–plastic deformation behavior is modeled by a nonlinear time-dependent dashpot in series with a linear elastic spring system, as shown in Fig. 8(right). Arranging a spring (e.g. linear) parallel to the dashpot results in a standard-like solid model (Kelvin–Voigt representation). Although an additional spring is known to improve creep predictions, it is useful only under permanently high stress levels (in relation to the ultimate strength), which rarely occurs in practice. Therefore, an additional spring was omitted to keep the model simple and efficient in practical use. Alternatively, by using the Kelvin–Voigt (1890) model (probably modified with a nonlinear spring and dashpot) between the elastic spring and nonlinear dashpot, the model becomes similar to the Burger model (1935) which is known to be capable of capturing the large and long-term deformation behavior of fiber-reinforced polymers. However, the nonlinear spring in the Kelvin–Voigt-like element preserves only notably large deformations which are omitted here. Moreover, the Burger model is more complex than the proposed Maxwell-like model.

To define the stress-free intermediate configuration uniquely, the viscoelastic–plastic spin is required to be zero, that is, $\bar{\boldsymbol{L}}^{\mathrm{vep}} = \mathrm{sym}(\bar{\boldsymbol{L}}^{\mathrm{vep}}) = \bar{\boldsymbol{D}}^{\mathrm{vep}}$ (in (5)) holds for the amorphous deformation (spin is small compared to $\bar{\boldsymbol{D}}^{\mathrm{vep}}$, if it itself is small [59]). Moreover, the total deformation was regarded to be small (less than 10%). In a departure from previous theories for polymeric materials [24,53,59], the viscoelastic–plastic rate of deformation is given by the sum of several micromechanisms. However, considering the restricted deformability of NSRF polymers, a single microsystem (single nonlinear dashpot in Fig. 8(right)) is considered to be sufficient to reproduce the nonlinear σ vs. ϵ response. The viscoelastic–plastic rate of deformation is then defined by

$$\bar{\boldsymbol{D}}^{\mathrm{vep}} = (\dot{\gamma}^{\mathrm{vep}}/(2\tau) - 1/\eta)(\tau/\tau_0)^{1/m}\boldsymbol{\sigma}^{\mathrm{dev}}, \tag{6}$$

where $\tau = \sqrt{1/2\mathrm{tr}\,(\boldsymbol{\sigma}^{\mathrm{dev}})^2}$ is the effective stress, m is the material parameter (the limit $m \to 0$ corresponds to the rate-independent limit), and the deviatoric part dev for each tensor $[\cdot]$ is defined by the identity $\boldsymbol{i}$ as $[\cdot]^{\mathrm{dev}} := [\cdot] - 1/3\mathrm{trace}([\cdot])\boldsymbol{i}$. The constant viscosity compliance $1/\eta$ is used to capture stress relaxation and creep and is constrained by the relation $\dot{\gamma}^{\mathrm{vep}}/(2\tau) - 1/\eta \geq 0$ ($\eta \sim 1 \cdot 10^4$ MPa-s); otherwise, $\bar{\boldsymbol{D}}^{\mathrm{vep}} = \boldsymbol{0}$. In the absence of this term, the proposed Maxwell-like model will result in excessive melt fluid at RT [60]. The latter term in parentheses corresponds to the strain rate dependence; the characteristic strength τ_0 equals with the effective stress for $\dot{\epsilon} \to 0$ (when $\sigma_{\mathrm{u}} \to 40$ MPa in tension).

The evolution of viscoelastic–plastic deformation was modeled using the following power-law-type strain rate [59]:

$$\dot{\gamma}^{\mathrm{vep}} = \dot{\gamma}_0^{\mathrm{a}}\Big(\frac{\tau}{s^{\mathrm{a}} - 1/3\varsigma I_1}\Big)^{1/m} \geq 0, \tag{7}$$

where $\dot{\gamma}_0^{\mathrm{a}}$ and ς are the material parameters, s^{a} is an internal state variable (representing the resistance to plastic shear flow [59]) and $I_1 = \mathrm{tr}\,(\boldsymbol{\sigma})$ is the first invariant of the stress indicating pressure; plastic deformation is suppressed under compression, that is, microcracks are opened in tension and partially closed in compression. Therefore, the proposed flow evolution equation for plastic deformation depends on the pressure, resulting in an asymmetry between tension and compression [23,59].

The evolution of plastic deformation (7) can mimic the microscopically motivated plastic evolution [61] for glassy polymers [62]. It is assumed that the influence of the ongoing relatively small viscous deformation (strain lower than 5%) on the molecular resistance is small when s^{a} is considered as a constant (represented by dashpot a) in Fig. 8(right). When the viscous deformation is sufficiently large (> 10%), s^{a} should be considered to depend on the porosity (void volume) and its time-dependent evolution [24,53,59]. The stress of the amorphous phase is given by

$$\boldsymbol{\sigma}^{\mathrm{a}} = (1-\xi)\mathfrak{L}^{e,a} : \ln \boldsymbol{v}^{\mathrm{e}} = (1-\xi)E^{\mathrm{a}}/(1+\nu^{\mathrm{a}})\ln \boldsymbol{v}^{\mathrm{e}} + (1-\xi)E^{\mathrm{a}}/[3(1-2\nu^{\mathrm{a}})]\mathrm{tr}\,(\ln \boldsymbol{v}^{\mathrm{e}})\boldsymbol{i}, \tag{8}$$

where E^{a} is the Young's modulus and ν^{a} is the Poisson ratio. In summary, the macroscopic viscoelastic–plastic deformation response is modeled by the minimum number of micro- to macroscopic internal variables and parameters. The isothermal aspects of the model, its numerical treatment, and its reduced presentations for creep and stress relaxation are all discussed in Appendix.

4. Results

Benchmark

The model parameters were extracted from the uniaxial monotonic tensile test results at RT. The average Young's modulus E of the composites (PLA + hemp 20%wt + PEG 1.5 - 20k plasticizers 0 - 5%wt in the printing direction) was extracted from the linear strain range (0–0.0025) of the $\sigma - \epsilon$ curve, as demonstrated in Fig. 6(left). The influence between the plasticizers PEG 1.5 - 20k was small, Fig. 10(left), and therefore not considered in the model. Similarly, Young's moduli of the matrix E^{m} (PLA, printed specimen) and its amorphous phase E^{a} (PLA specimen produced by extrusion [63]) were determined from their initial responses. The Young's moduli of the fiber E^{f} and the crystalline phase E^{c} were then calculated from relations [a] and [b] described above. Using the calibrated values, $E^{\mathrm{f}} \approx 8,100$ MPa (hemp) was obtained, which represents the average modulus in the three main directions [57]. The difference of the Poisson's ratios between the different phases and the fibers were considered small, that is the unified values $\nu^{\mathrm{f}} = \nu^{\mathrm{c}} = \nu^{\mathrm{a}} = \nu$ were used.

The compact set of model parameters for viscoelastic–plastic deformation is comprised by $\dot{\gamma}_0^{\mathrm{a}}$, β, m, s^{a}, and the viscosity of the composite η. The s^{a} parameter is an internal state variable representing the molecular resistance to plastic shear flow, and its value for the macroscopic σ vs. ϵ response corresponds to the stress value when nonlinear plastic deformation begins to develop (~ 25 MPa in Fig. 10(left)) [53,64]. The initial values of the parameters $\dot{\gamma}_0^{\mathrm{a}}$, β, and m were obtained based on previous studies of polymers [59] and their values were refined over several iterations. The viscosity of the composite η at RT was available neither from experiments performed in this work nor from the reports in the literature. Therefore, η was first deduced from the viscosities of melted PLA (~ 6 kPa s [65]), PEG at RT (~ 0.1–1 kPa s [66]), hemp at RT (~ 1 kPa s [67]), and their melt composites (~ 6 kPa s [68]). However, the viscosity of PLA with high content of 75–80%wt in the composite shows an exponential increase with decreasing temperature, even in the melt phase (over 150 °C) [65,69]. Therefore, a higher η magnitude was used to predict the macroscopic deformation at RT (T denotes the temperature): $\eta = A\exp(-BT^n) = 7...$infinity MPa s, where $A = 2{\cdot}10^7...$infinity MPa s and $B = 50...6,700$ (°C)$^{1/n}$ when $n = 1...2$ (data values $\eta(170\,^{\circ}\mathrm{C}) = 2.9$ kPa s and $\eta(150\,^{\circ}\mathrm{C}) = 8.2$ kPa s were used [69]). The final set of the model parameters is listed in Table 1.

Model predictions vs. experimental data

The viscoplastic logarithmic strain governs the total deformation, as shown in Fig. 10(top left), and the elastic strain limit $\epsilon^{\mathrm{e}} \sim 0.004$ is also observed. Although the fibers and the amorphous and crystalline phases jointly contribute to the material strength [70], the highly nonlinear macroscopic stress–strain behavior (plastic toughness) is mainly affected by the entangled network of the amorphous phase and sufficient

Table 1
Model parameters for the NSFR polymer used (PLA + hemp 20%wt + PEG plasticizer 0 - 5%wt at RT).

Parameter	E	ν	E^{m}	E^{a}	$\dot{\gamma}_0^{a}$	ς	m	s^{a}	η
Unit	MPa		MPa	MPa	s-1			MPa	MPa s
Value	3600	0.37	3200	3000	0.004	0.2	0.11	26	40,000

porosity of the composite (8%–9%), and the viscoplastic deformability and ductility are significantly reduced with decreasing porosity (see the red curve in Fig. 10(top left)).

The results presented in Fig. 10(top left) indicate that the incorporation of the proposed nonlinear viscous dashpot for governing viscous micromechanisms enables the capture of the overall trends of the highly nonlinear loading responses of the composites. These predictions could be further improved by neglecting the brittle composite without plasticizers (used in the model fitting). Notably, high non-linearity of the responses at small applied strains of 0.5%–3% is observed, and the observed ultimate tensile strength $\sigma_u \sim 40$ MPa is typical of the PLA-hemp composites [37]. Fig. 10(top right) further shows the variation of the stress vs. strain when the relevant values of the essentially independent variables (porosity, DC, fiber content) are used. When particularly the fiber content decreased and the porosity increased, both the experimental and model results show an increased plastic deformability [71]. However, experimental results also shows a brittleness, that is, a reduction in the strain due to damage of the material and rupture of the test specimens. It is concluded that in further research, the mathematical model should be augmented by a suitable damage model that can predict material failure for reduced porosity. Nevertheless, the predicted nonlinear unloading response is typical of amorphous and semi-crystalline polymers [62,72,73] and short (E-glass) fiber-reinforced thermoplastics [17]. No recovery was measured nor predicted after load removal at zero stress for one day, which is characteristic of the viscoplastic response (showing a permanent residual strain) under small strains.

In addition, any capable model is required to provide strain rate dependence and reasonable predictions of creep and stress relaxation at different stress and strain levels, respectively. Fig. 10(bottom left) shows measured and predicted strain rate dependencies ranging between 0.001/s and ~2100/s. At the ultimate of the (dynamic) strain rate, the model predictions are quite linear, capturing the data on average. The observed accumulated reduction of stress at the high strain rates has been reported to be due to the hemp fibers that are perpendicular to the direction of the stress and delay as empty space or failure locations without a marked aid in the response of the composite [74]. The model shows significant nonlinear plastic deformation when the strain rate is ~50/s, and the predictions are highly accurate when the strain rate is small, less than 0.01/s. The model predictions slightly violates from the data for the intermediate strain rate range (~1/s - 100/s) essentially because the stiffer specimen (standard ISO 527-4 type 1B ~ ASTM D638 type I specimen: larger thickness and curvature between the hold and gauge sections) has been used under the strain rates less than 1/s [75].

Fig. 10(bottom right) further shows the creep responses at different fixed, relatively low stress levels, σ_0, that are relevant for practical applications. The creep strain depends strongly on σ_0, increasing essentially linearly with σ_0 [76], and at the lowest stress level (approximately 35% of the ultimate tensile strength), the creep strain is suppressed. This creep behavior is in agreement with the observed behavior of polymers [62,72,73]. Finally, Fig. 11 shows the stress relaxation at different fixed strain levels ϵ_0: stress relaxation is significant and is a nonlinear function of the applied ϵ_0. The stress asymptotically approaches the limit $\bar{\sigma} = 15.5$ MPa. Comparison with pure PLA shows that the model predictions are accurate (the PLA in the composite governs the nonlinear plastic deformation, and thus, relaxation). A comparison with high-strength PLA-PCL (PolyCaproLactone) composite [77] shows that the predicted relaxation development at higher ϵ_0 is still realistic.

Predicted data vs. ML

Research studies typically encounter the problem of insufficient availability of costly experimental data for investigations of all of the conditions of interest. In our case, majority of the history-dependent data for unloading, creep, and stress relaxation were unavailable. Nevertheless, the available minimal data set allowed for model validation as was discussed above, and the model is used to provide missing experimental data. However, constitutive mathematical modeling is computationally time-consuming when applied to predict long-term deformation behaviors, such as creep, relaxation, and fatigue, whereas ML methods are computationally very efficient. Therefore, an approach where the proposed mathematical model is solely used to produce training data for ML is proposed. By replacing the unavailable experimental data with predicted high-quality model data (obtained from an advanced microstructural-based model calibrated to the available experimental data), one can generate unlimited amount of data for ML and then, construct as-build models of real-life objects [79] and digital (numerical) twins [80]. Fig. 12 illustrates the proposed concept based on ML which is trained using both the available experimental data and the predicted high-quality model data.

Remark. *Compared to conventional concepts where the ML is solely based on the available and costly experimental data, the ML in the proposed concept is based on a suitable combination of the predicted, high-quality model data and the available experimental data. Data generated implicitly by ML (e.g. by the neural networks or DMN) are out of the scope of this work.*

We demonstrated a proof-of-concept example of this approach in which the macroscopic deformation behavior of NSFR polymers (σ vs. ϵ response) was investigated, and the experimental data for unloading and stress relaxation were unavailable. Therefore, the proposed compact and advanced mathematical model was used to predict the missing data for the ML training. The tensile stress σ (vs. strain ϵ) was the target property of the ML prediction and was shown to depend strongly and nonlinearly on the porosity, DC, and fiber content. For ML, it is necessary to first investigate the correlations among these material variables. The Pearson correlation is the best-known correlation measure and is given by

$$\rho_{xy} = \frac{n(\Sigma x_i y_i) - (\sum x_i)(\sum y_i)}{\sqrt{n\sum x_i^2 - (\sum x_i)^2}\sqrt{n\sum y_i^2 - (\sum y_i)^2}}, \tag{9}$$

where x_i and y_i are the individual values of material variables and n is the product of the range of these values. In other words, the Pearson correlation shows the mutual correlation between two variables x and y. In this case, the porosity, DC, and fiber content, representing the material variables, varied between 4 and 9%, 30 and 39%, and 20 and 30%wt respectively, and the values of the variables were constrained by these limits. Then, for instance, $n = (0.04-0.09)\cdot(0.30-0.39) = 0.004$ is the product of the value ranges for the porosity and DC (x and y). Table 2 lists the correlation values of the different pairs of material variables based on the Pearson correlation (9): The correlations between the variables are very low, indicating that these variables are essentially independent of each other. The largest correlation was found between DC and fiber content, and both of these material variables had a negligible correlation with the porosity.

To improve the ML process, it is important to investigate the variables' importance. The random forest (RF) algorithm is a suitable

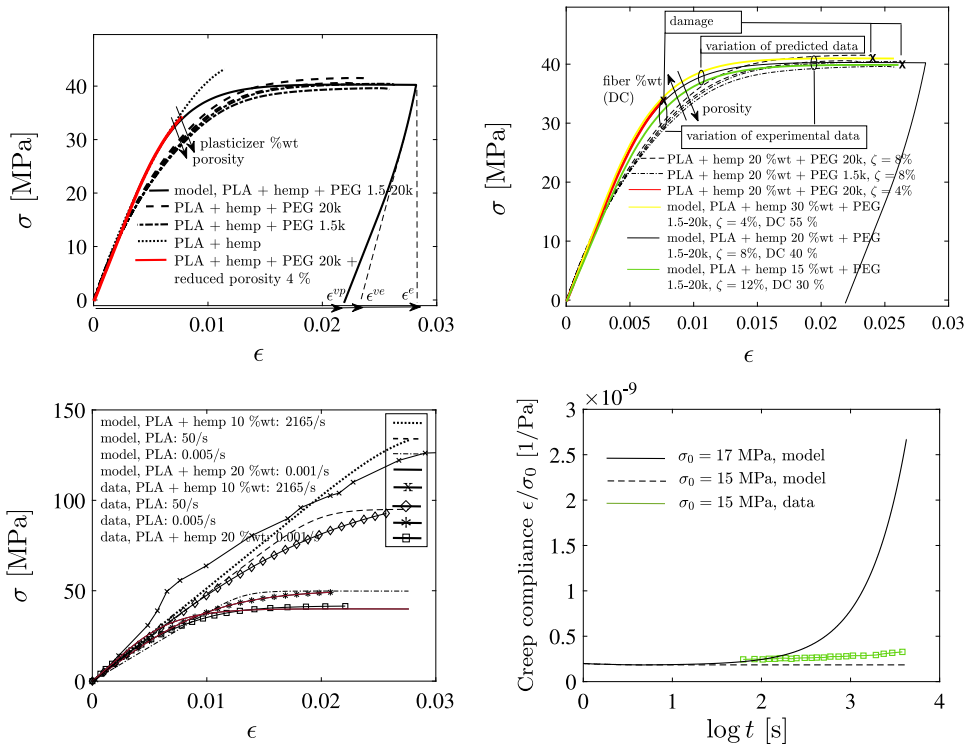

Fig. 10. Predicted (solid) and measured stress (up to rupture of the specimens) vs. strain responses in the printing direction (0°) (top left). Thin dashed straight lines demonstrate the (visco)elastic strains after unloading. Predicted and measured responses (up to rupture due to damage highlighted by the marker x) depending on the porosity ζ, DC, and fiber content (in the printing direction, 0^0) (top right). Measured (mean values up to rupture) [74,75] and modeled strain rate dependencies (bottom left). The strain rate $\dot{\epsilon} = 2165/s$ is for compression, all others are for tension. Predicted (black) creep strains (at $\dot{\epsilon} = 0.001/s$) for different initial stresses $\sigma_0 \sim \sigma_u/(2.5...3)$ during the time period of 1 h (bottom). Corresponding measured (green) response for similar composite (PLA + hemp 20 %wt [76]; $\sigma_0 \sim \sigma_u/3$) is also shown.

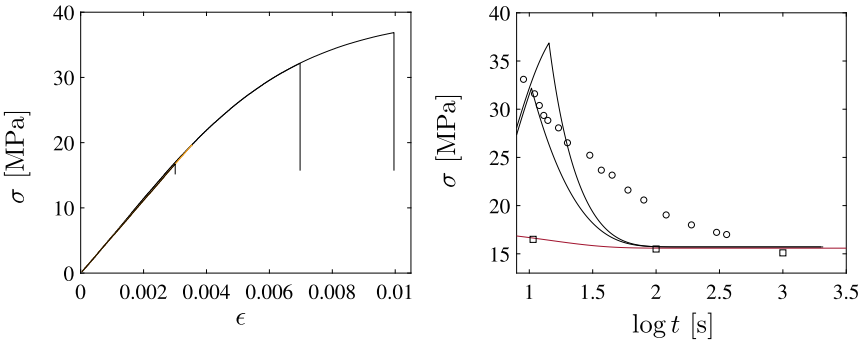

Fig. 11. Predicted σ vs. ϵ responses of the composite for the stress relaxation (at $\dot{\epsilon} = 0.001/s$) during 1 h (left). Corresponding time vs. stress responses (right). For comparison, data points of the PLA-PCL composite (marked by ∘ for the initial strain $\epsilon_0 \sim 0.1$ [77]) and 3D-printed PLA (marked by □ [78]) are also shown.

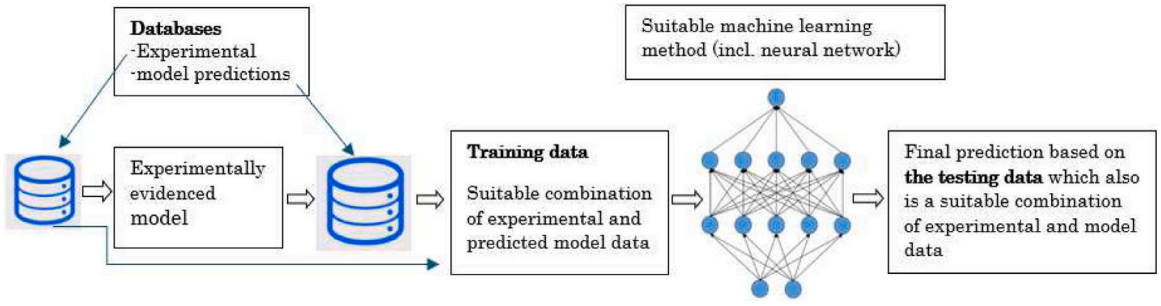

Fig. 12. Proposed approach based on ML boosted by high-quality data obtained by advanced (explicit) design modeling and experimental data, collected separately.

Table 2
Pearson correlation matrix for the NSFR polymer (PLA + hemp + PEG 1.5 - 20k 5%wt).

Parameter	Porosity	DC	Fiber content
porosity	1	0.004	0.004
DC	0.004	1	0.012
fiber content	0.004	0.012	1

method for this purpose, which pursues the average decrease in the impurity across all trees in the so-called forest resulting from splits of the specific feature (mean decrease in impurity, MDI) [81]. However, in this case study, the application of such an autonomous method is probably unnecessary because the mutual importance between the variables is known, and the experiments show that the deformation behavior of NSFR polymers depends mostly on the fiber content and porosity, whereas DC has little influence on the fiber content and porosity.

Due to the strong dependence of the σ vs. ϵ relationship on (independent) material variables, a suitable ML method must be selected [27,81]. For instance, traditional (unsupervised) methods based on linear regression (LR) and least absolute shrinkage operator (LASSO) methods [81] are not suitable, and more advanced (supervised) methods such as support vector regression (SVR) are preferred. SVR is widely used method because in contrast to LR, it can handle complex and weak relationships between the applied variables [82]. In contrast to LR, SVR seeks to construct a nonlinear function that can best fit the available data while minimizing the errors [83]. Because advanced ML methods such as SVR (based on neural networks) are based solely on the training data they show significant advantages including the lack of prior assumptions, comprehensive adaptability (for various materials and loading situations), and high computational efficiency. However, these methods also have some limitations [31]: [1] their accuracy depends strongly on the amount and quality of the training data (while the experimental data are expensive and limited), [2] the results of experiments and the numerical simulations usually exhibit a Gaussian distribution [30], while the ML methods do not satisfactorily reproduce such a distribution. Therefore, an improved ML approach was used in this work.

Improved ML approach

Recent advanced (ensemble) methods use a combination of multiple ML models to improve overall predictability. Examples of ensemble methods include gradient-boosting regression (GBR) and stacking [81]. Stacking is probably the most accurate approach, because it involves the training of base models and the use of their predictions as inputs for metamodel predictions. Based on previous findings for complex systems [81], the use of two or three base models may be sufficient, and the preferred methods can be a combination of unsupervised and supervised methods (LR, RF, SVR, GBR). Metamodels for final predictions should be based on supervised models (RF, SVR, GBR).

In the proposed approach for stacking, both the training data (for training the base models and the first-level meta-model) and the testing data (for validating the base models, first-level meta-model, and finally, the second-level meta-model) are based on a suitable combination of the unlimited amount of the predicted model data and the relatively few available experimental data (see Fig. 13). Stacking was further reduced such that the first-level meta-model was solely based on a single-base model using the SVR (based on random splitting). Moreover, the first meta-model was the final model used in the final predictions. This reduced approach was robust for the investigation of highly nonlinear strain-versus-stress relationships, whereas use of several unsupervised base models resulted in inaccurate predictions.

Fig. 14 shows the ML predictions (based on the reduced stacking) for the nonlinear loadings of the NSFR polymer (PLA + hemp 20%wt + PEG 1.5 - 20k), for the porosity, DC, and fiber content of 8%, 38% (average value corresponding to the experimental data), and 20%wt, respectively. For training and testing the SVR for monotonic loading, all of the data were the experimental data listed in Table 3. For unloading, when no experimental data were available, SVR was trained using only the model data. For stress relaxation (including the two responses shown in Fig. 14(right)), for which the experimental data were scarce, 75% of the training data were the predicted model data. Based on the previous experience of the effectiveness of the SVR [81,82] improved by stacking, it is not surprising that ML shows accurate predictions for both unloadings and stress relaxation because the learning during the unloadings and the stress relaxation was carried out with abundant predicted model data. The total CPU elapsed time for the mathematical constitutive model, employing a maximum constant time increment within the implicit backward Euler integration scheme with quadratic convergence, was reduced by more than 90% when the ML was used (with both training and testing phases).

5. Conclusion

This article describes experiments used to investigate the highly nonlinear, plastic deformation behavior of NSFR polymers (test specimens were manufactured by 3D-printing with P-MEX), their mathematical modeling with a physically motivated model calibrated using the experimental data, and the application of the model predictions as training data for the ML model. Because of the compact formulation, the proposed mathematical, cutting-edge model is easy to implement and was used to predict an unlimited amount of data for training of advanced ML methods such as SVR and stacking. The proposed numerical databases, which consist of advanced model predictions, promote building of digital (numerical) twins and provide unlimited data for ML models that are highly efficient in predicting extremely long-term deformation and fatigue processes. With this approach, low cost product development of bio-based materials can be enhanced using the optimal combination of experiments, advanced mathematical modeling, and ML predictions.

CRediT authorship contribution statement

N. Niang: Writing – original draft, Validation, Methodology, Investigation, Formal analysis, Data curation, Conceptualization. **T. Barriere:** Validation, Supervision, Resources, Project administration, Investigation, Funding acquisition. **X. Gabrion:** Validation, Software, Methodology, Data curation. **S. Holopainen:** Writing – original draft, Supervision, Software, Resources, Investigation, Conceptualization. **V. Placet:** Validation, Supervision, Resources, Project administration, Methodology, Formal analysis, Data curation, Conceptualization.

Declaration of competing interest

The authors declare that they have no known competing financial interests or personal relationships that could have appeared to influence the work reported in this paper.

Acknowledgments

This work was supported by the EIPHI Graduate School (Contract ANR-17-EURE-0002). The authors thank the IT Center for Science Ltd. (CSC, Finland) for providing the computational resources. The authors thank MIFHySTO and AMETISTE platforms (UMLP, France) for providing test equipment.

Table 3
The data (in ascii -format) used for the ML. The fiber (hemp) content is 20%wt.

Data index	Composite	Content
expdata1	PLA + hemp + SA 0...5%wt	experimental, monotonic loading
expdata2	PLA + hemp + PEG 1.5k 5%wt	experimental, monotonic loading
expdata3	PLA + hemp + PEG 1.5k 5%wt	experimental, monotonic loading
expdata4	PLA + hemp + PEG 20k 5%wt	experimental, monotonic loading
expdata5	PLA + hemp + PEG 20k 5%wt	experimental, monotonic loading
expdata6	PLA	experimental, monotonic load followed by stress relaxation from $\epsilon = 0.003$[a]
moddata1	PLA + hemp + PEG 1.5...20k 5%wt	predicted, monotonic load followed by unloading from $\epsilon = 0.0075$
moddata2	PLA + hemp + PEG 1.5...20k 5%wt	predicted, monotonic load followed by unloading from $\epsilon = 0.028$
moddata3	PLA + hemp + PEG 1.5...20k 5%wt	predicted, monotonic load followed by unloading from $\epsilon = 0.015$
moddata4	PLA + hemp + PEG 1.5...20k 5%wt	predicted, monotonic load followed by stress relaxation from $\epsilon = 0.01$
moddata5	PLA + hemp + PEG 1.5...20k 5%wt	predicted, monotonic load followed by stress relaxation from $\epsilon = 0.007$
moddata6	PLA + hemp + PEG 1.5...20k 5%wt	predicted, monotonic load followed by stress relaxation from $\epsilon = 0.003$

[a] Relevant data since the PLA governs the viscosity of the composites.

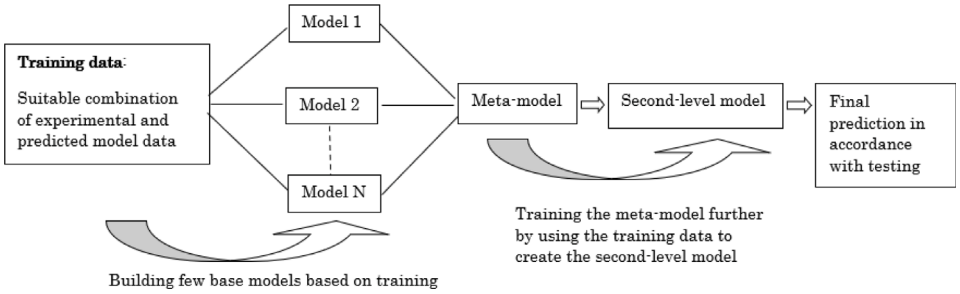

Fig. 13. Flowchart of the general stacking method.

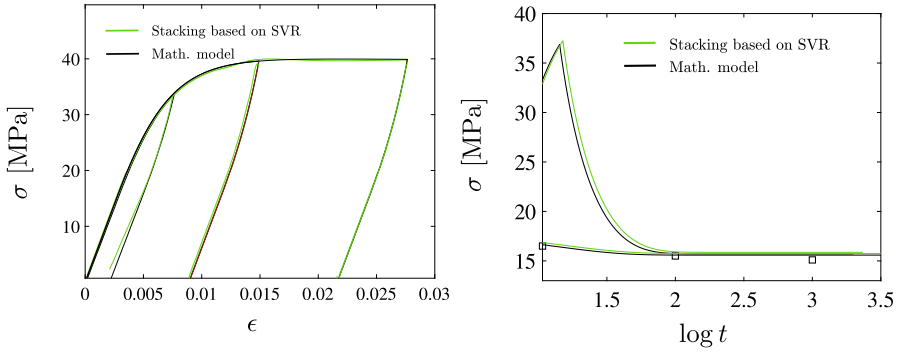

Fig. 14. Mathematical model predictions (black solid) and ML predictions [stacking based on the SVR] (green solid) (left). The mathematical model and ML predictions during the last unloading overlap. Predicted stress relaxation during 1 h (right). The observed data points (□) are also shown.

Appendix. Treatment of the mathematical model

Isothermal relevancy

The theory for irreversible, dissipative, and prolonged effects (nonlinear loading and unloading responses, creep, and stress relaxation) governing viscoelastic–plastic deformations is based on the virtual power balance obeying two assumptions: Power balance (the internal and external virtual powers are equal) and the internal power is frame-indifferent, i.e., invariant under all changes in a frame of the space (Euclidean). To treat these assumptions as well as the force and moment balances (stress symmetry), which are the consequences of expenditure of the external virtual power, we refer to previous works [56,59].

Frame-indifference

We consider time-dependent transformations at position $\boldsymbol{X}$ and time t as follows:

$$\boldsymbol{y}(\boldsymbol{X},t) \rightarrow \boldsymbol{q}(t) + \boldsymbol{Q}(t)(\boldsymbol{y}(\boldsymbol{X},t) - \boldsymbol{O}) \tag{A.1}$$

where $\boldsymbol{O}$ is a fixed origin, $\boldsymbol{q}(t)$ is a vector, and $\boldsymbol{Q}(t)$ is an orthogonal rotation tensor, for which $\boldsymbol{Q}^{-1} = \boldsymbol{Q}^{\mathrm{T}}$ holds. The reference placement (including the position $\boldsymbol{X}$) is considered to be invariant, whereas the current and intermediate placements depend on the choice of changes in frame, i.e.,

$$\boldsymbol{F} \rightarrow \boldsymbol{Q}\boldsymbol{F}, \quad \boldsymbol{F}^{\mathrm{vep}} \rightarrow \bar{\boldsymbol{Q}}\boldsymbol{F}^{\mathrm{vep}}, \quad \boldsymbol{F}^{\mathrm{e,x}} \rightarrow \boldsymbol{Q}\boldsymbol{F}^{\mathrm{e,x}}\bar{\boldsymbol{Q}}^{\mathrm{T}} \tag{A.2}$$

for all x = a, f, c (a = amorphous phase, f = fiber, c = crystalline phase), where $\boldsymbol{F}^{\mathrm{e,x}} = \boldsymbol{F}^{\mathrm{e}}$ (accordance with the idea of the model demonstrated in Fig. 8(right)), and $\boldsymbol{Q}$ and $\bar{\boldsymbol{Q}}$ represent the rotations of the current and intermediate placements, respectively. Subsequently, the applied deformation measure $\boldsymbol{b}^{\mathrm{e}} = \boldsymbol{v}^{\mathrm{e}}\boldsymbol{v}^{\mathrm{e}} = \boldsymbol{F}^{\mathrm{e}}\boldsymbol{F}^{\mathrm{e,T}}$ is transformed as follows:

$$\boldsymbol{b}^{\mathrm{e}} \rightarrow \boldsymbol{Q}\boldsymbol{b}^{\mathrm{e}}\boldsymbol{Q}^{\mathrm{T}} \tag{A.3}$$

in the current placement and the transformations $(A.2)_{1,2}$ in (5) result in

$$\begin{aligned} &\bar{\boldsymbol{L}}^{\mathrm{vep}} \rightarrow \bar{\boldsymbol{Q}}\bar{\boldsymbol{L}}^{\mathrm{vep}}\bar{\boldsymbol{Q}}^{\mathrm{T}} + \dot{\bar{\boldsymbol{Q}}}\bar{\boldsymbol{Q}}^{\mathrm{T}}, \quad \bar{\boldsymbol{D}}^{\mathrm{vep}} \rightarrow \bar{\boldsymbol{Q}}\bar{\boldsymbol{D}}^{\mathrm{vep}}\bar{\boldsymbol{Q}}^{\mathrm{T}}. \\ &\boldsymbol{L}^{\mathrm{vep}} \rightarrow \boldsymbol{Q}\boldsymbol{L}^{\mathrm{vep}}\boldsymbol{Q}^{\mathrm{T}} - \boldsymbol{Q}\boldsymbol{F}^{\mathrm{e}-\mathrm{T}}\dot{\boldsymbol{Q}}^{\mathrm{T}}\bar{\boldsymbol{Q}}\boldsymbol{F}^{\mathrm{e}-1}\boldsymbol{Q}^{\mathrm{T}}, \quad \boldsymbol{D}^{\mathrm{vep}} \rightarrow \boldsymbol{Q}\boldsymbol{D}^{\mathrm{vep}}\boldsymbol{Q}^{\mathrm{T}} \end{aligned} \tag{A.4}$$

for intermediate and current placements, respectively. To obtain the results, the property $\bar{\boldsymbol{Q}}^{\mathrm{T}}\dot{\bar{\boldsymbol{Q}}} = -\dot{\bar{\boldsymbol{Q}}}^{\mathrm{T}}\bar{\boldsymbol{Q}}$ was used [56].

In accordance with (5) for viscoelasto-plasticity, the elastic velocity gradient $\boldsymbol{L}^{\mathrm{e}}$ defines the evolution of the elastic deformation gradient as

$$\dot{\boldsymbol{F}}^{\mathrm{e}} = \boldsymbol{L}^{\mathrm{e}}\boldsymbol{F}^{\mathrm{e}}. \tag{A.5}$$

The last transformation in (A.2) applied in (A.5) results in ($\boldsymbol{F}^{\mathrm{e,x}} = \boldsymbol{F}^{\mathrm{e}}$)

$$\boldsymbol{L}^{\mathrm{e}} \to \boldsymbol{Q}\boldsymbol{L}^{\mathrm{e}}\boldsymbol{Q}^{\mathrm{T}} + \dot{\boldsymbol{Q}}\boldsymbol{Q}^{\mathrm{T}} + \boldsymbol{Q}\boldsymbol{F}^{\mathrm{e-T}}\dot{\bar{\boldsymbol{Q}}}^{\mathrm{T}}\bar{\boldsymbol{Q}}\boldsymbol{F}^{\mathrm{e-1}}\boldsymbol{Q}^{\mathrm{T}} \tag{A.6}$$

for all x = a, f, c. Noting the multiplicative decomposition (2) in the evolution $\dot{\boldsymbol{F}} = \boldsymbol{L}\boldsymbol{F}$ yields $\boldsymbol{L} = \boldsymbol{L}^{\mathrm{e}} + \boldsymbol{L}^{\mathrm{vep}}$ [51,56,59].

Suppose that the virtual velocity fields $\mathfrak{V}^*$ of a part of the solid body $\mathfrak{A}^*$ transform in the similar manner to their non-virtual counterparts $\mathfrak{V}$ and $\mathfrak{A}$, then assumption [strong bonding between fibers and the matrix] implies that in the current frame, $\mathfrak{W}^{\mathrm{int}}(\mathfrak{A},\mathfrak{V}) = \mathfrak{W}^{\mathrm{int}*}(\mathfrak{A}^*,\mathfrak{V}^*)$. Similarly, the stress field $\boldsymbol{\tau}$ (by Kirchhoff, $\boldsymbol{\tau} = \det(\boldsymbol{F})\boldsymbol{\sigma} \sim \boldsymbol{\sigma}$ with small strains <10% [51]) transforms into $\boldsymbol{\tau}^*$ conjugate to the virtual velocities when, noting (A.4) and (A.6),

$$\mathfrak{W}^{\mathrm{int}}(\mathfrak{A},\mathfrak{V}) := \int_{\mathfrak{A}} \boldsymbol{\tau} : \boldsymbol{L}dv = \mathfrak{W}^{\mathrm{int}*}(\mathfrak{A}^*,\mathfrak{V}^*) := \int_{\mathfrak{A}} \boldsymbol{\tau}^* : (\boldsymbol{Q}\tilde{\boldsymbol{L}}\boldsymbol{Q}^{\mathrm{T}} + \dot{\boldsymbol{Q}}\boldsymbol{Q}^{\mathrm{T}})dv, \tag{A.7}$$

where $\boldsymbol{A} : \boldsymbol{B} := \mathrm{trace}(\boldsymbol{A}\boldsymbol{B})$, and the results

$$\begin{aligned} &\boldsymbol{\tau} : \boldsymbol{L}^{\mathrm{e}} \to \boldsymbol{\tau} : (\boldsymbol{Q}\boldsymbol{L}^{\mathrm{e}}\boldsymbol{Q}^{\mathrm{T}} + \dot{\boldsymbol{Q}}\boldsymbol{Q}^{\mathrm{T}}) + \bar{\boldsymbol{T}} : \dot{\bar{\boldsymbol{Q}}}^{\mathrm{T}}\bar{\boldsymbol{Q}}, \\ &\boldsymbol{\tau} : \boldsymbol{L}^{\mathrm{vep}} \to \boldsymbol{\tau} : \boldsymbol{Q}\boldsymbol{L}^{\mathrm{vep}}\boldsymbol{Q}^{\mathrm{T}} - \bar{\boldsymbol{T}} : \dot{\bar{\boldsymbol{Q}}}^{\mathrm{T}}\bar{\boldsymbol{Q}} \end{aligned} \tag{A.8}$$

were used. Because the body part $\mathfrak{A}$ is arbitrary, (A.7) can be localized, i.e. $\boldsymbol{\tau} : \boldsymbol{L} = \boldsymbol{\tau}^* : (\boldsymbol{Q}\tilde{\boldsymbol{L}}\boldsymbol{Q}^{\mathrm{T}} + \dot{\boldsymbol{Q}}\boldsymbol{Q}^{\mathrm{T}})$ holds. Because the change in frame, $\tilde{\boldsymbol{L}}$, as well as $\dot{\boldsymbol{Q}}\boldsymbol{Q}^{\mathrm{T}} = -\boldsymbol{Q}\dot{\boldsymbol{Q}}^{\mathrm{T}}$ (skew-symmetric) are arbitrary, the stress (symmetric) transforms by $\boldsymbol{\tau} \to \boldsymbol{Q}\boldsymbol{\tau}\boldsymbol{Q}^{\mathrm{T}}$, and the stress $\bar{\boldsymbol{T}} := \boldsymbol{F}^{\mathrm{e-1}}\boldsymbol{\tau}\boldsymbol{F}^{\mathrm{e-T}}$ in (A.8) is the counterpart of $\boldsymbol{\tau}$ given in the intermediate placement [56]. That is, the push-forward operator for kinetic (stress-like) quantities is $\phi_* = \boldsymbol{F}^{\mathrm{e}}(\cdot)\boldsymbol{F}^{\mathrm{e,T}}$, which is in accordance with the previous works [51, Box. 5.16]. Furthermore, considering the symmetry of $\boldsymbol{\tau}$ yields $\boldsymbol{\tau} : \boldsymbol{L} = \boldsymbol{\tau} : (\boldsymbol{L}^{\mathrm{e}} + \boldsymbol{L}^{\mathrm{vep}}) = \boldsymbol{\tau} : (\boldsymbol{D}^{\mathrm{e}} + \boldsymbol{D}^{\mathrm{vep}}) = \boldsymbol{\tau} : \boldsymbol{D}$.

Constitutive theory

Based on the above results, and noting the approach of the model shown in Fig. 8(right), the power of the local dissipation $\mathcal{D}$ in its spatial form becomes

$$\mathcal{D} = \boldsymbol{\tau} : \boldsymbol{D}^{\mathrm{e}} + \boldsymbol{\tau} : \boldsymbol{D}^{\mathrm{vep}} - \dot{\psi} = (\boldsymbol{\tau}^{\mathrm{a}} + \boldsymbol{\tau}^{\mathrm{f}} + \boldsymbol{\tau}^{\mathrm{c}}) : \boldsymbol{D}^{\mathrm{e}} + \boldsymbol{\tau} : \boldsymbol{D}^{\mathrm{vep}} - \dot{\psi} \geq 0, \tag{A.9}$$

or

$$\mathcal{D} = \sum\nolimits_{\mathrm{x=a,f,c}} \boldsymbol{\tau}^{\mathrm{x}} : \boldsymbol{D}^{\mathrm{e}} + \boldsymbol{\tau} : \boldsymbol{D}^{\mathrm{vep}} - \dot{\psi} \geq 0, \tag{A.10}$$

where $\dot{\psi}$ stands for the rate of the Helmholtz free energy per unit volume. The Helmholtz free energy ψ is considered as the sum of several independent potentials [59,84],

$$\psi = \hat{\psi}(\boldsymbol{b}^{\mathrm{e}}) = \sum\nolimits_{\mathrm{x=a,f,c}} \hat{\psi}^{\mathrm{e,x}}(\boldsymbol{b}^{\mathrm{e}}), \tag{A.11}$$

where $\psi^{\mathrm{e,x}}$ are the contributions associated with the elastic springs b), c), and d) in Fig. 8(right). The rate $\dot{\varphi}$ is given by

$$\dot{\psi} = \sum\nolimits_{\mathrm{x=a,f,c}} \frac{\partial \psi^{\mathrm{e,x}}}{\partial \boldsymbol{b}^{\mathrm{e}}} : \dot{\boldsymbol{b}}^{\mathrm{e}}. \tag{A.12}$$

Taking advantage of

$$\dot{\boldsymbol{b}}^{\mathrm{e}} = \boldsymbol{L}^{\mathrm{e}}\boldsymbol{b}^{\mathrm{e}} + \boldsymbol{b}^{\mathrm{e}}\boldsymbol{L}^{\mathrm{e,T}} \tag{A.13}$$

(based on $\boldsymbol{b}^{\mathrm{e}} = \boldsymbol{F}^{\mathrm{e}}\boldsymbol{F}^{\mathrm{e,T}}$ in (A.5)), noting the symmetry of $\boldsymbol{b}^{\mathrm{e}}$, and considering $\psi^{\mathrm{e,x}}$ as an isotropic function of $\boldsymbol{b}^{\mathrm{e}}$ result in

$$\frac{\partial \psi^{\mathrm{e,x}}}{\partial \boldsymbol{b}^{\mathrm{e}}} : \dot{\boldsymbol{b}}^{\mathrm{e}} = 2\frac{\partial \psi^{\mathrm{e,x}}}{\partial \boldsymbol{b}^{\mathrm{e}}}\boldsymbol{b}^{\mathrm{e}} : \boldsymbol{D}^{\mathrm{e}}. \tag{A.14}$$

The complementary dissipation power is associated with the viscoelastic–plastic dashpot (a) in Fig. 8(right), $\phi^{\mathrm{vep}}(\boldsymbol{\tau})$ where $\boldsymbol{\tau}$ denotes the driving stress in the dashpot. Benefiting the potential ϕ, the viscoelastic–plastic portion of the dissipation power becomes:

$$\frac{\partial \phi^{\mathrm{vep}}}{\partial \boldsymbol{\tau}} : \boldsymbol{\tau}. \tag{A.15}$$

Considering (A.12), substituting (A.14) and (A.15) into (A.10) results in

$$\begin{aligned} &\sum\nolimits_{\mathrm{x=a,f,c}} \left(\boldsymbol{\tau}^{\mathrm{x}} - 2\frac{\partial \psi^{\mathrm{e,x}}}{\partial \boldsymbol{b}^{\mathrm{e}}}\boldsymbol{b}^{\mathrm{e}}\right) : \boldsymbol{D}^{\mathrm{e}} = 0, \\ &\boldsymbol{\tau} : \boldsymbol{D}^{\mathrm{vep}} - \frac{\partial \phi^{\mathrm{vep}}}{\partial \boldsymbol{\tau}} : \boldsymbol{\tau} = 0. \end{aligned} \tag{A.16}$$

Eq. (A.16) must be valid under any possible thermodynamically admissible mechanism when the constitutive equations

$$\boldsymbol{\tau}^{\mathrm{x}} = 2\frac{\partial \psi^{\mathrm{e,x}}}{\partial \boldsymbol{b}^{\mathrm{e}}}\boldsymbol{b}^{\mathrm{e}} \tag{A.17}$$

for all x = a,f,c, and

$$\boldsymbol{D}^{\mathrm{vep}} = \frac{\partial \phi^{\mathrm{vep}}}{\partial \boldsymbol{\tau}} \tag{A.18}$$

are obtained. In accordance with (6),

$$\begin{aligned} \boldsymbol{\tau} : \boldsymbol{D}^{\mathrm{vep}} = \frac{\partial \phi^{\mathrm{vep}}}{\partial \boldsymbol{\tau}} : \boldsymbol{\tau} = (\dot{\gamma}^{\mathrm{vep}}/\tau - 1/\eta)(\tau/\tau_0)^{1/m}\boldsymbol{\tau}^{\mathrm{dev}} : \\ \boldsymbol{\tau} = (\frac{\dot{\gamma}^{\mathrm{vep}}}{\sqrt{2}}\tau - \frac{\tau^2}{2\eta})(\tau/\tau_0)^{1/m} \geq 0. \end{aligned} \tag{A.19}$$

Because $\dot{\gamma}^{\mathrm{vep}}/\tau - 1/\eta \geq 0$ is required, part of the dissipation power (A.19) is equal to or greater than zero; consequently (noting (A.16)), the dissipation power $\mathcal{D}$ (A.9) is always equal to or greater than zero.

Distinct constitutive equations for elasticity

The elastic isotropic strain energy function is

$$\psi^{\mathrm{e,x}} = \frac{1}{2}\kappa^{\mathrm{e,x}}(I_1^{\mathrm{e}})^2 + 2\mu^{\mathrm{e,x}}J_2^{\mathrm{e}}, \tag{A.20}$$

where $\kappa^{\mathrm{e,x}}$ and $\mu^{\mathrm{e,x}}$ denote the bulk and shear moduli for all x = a,f, and c, respectively (St. Venant–Kirchhoff materials, [51]). The invariants in (A.20) are given by

$$I_1^{\mathrm{e}} := \mathrm{trace}(\ln \boldsymbol{v}^{\mathrm{e}}) = \ln J^{\mathrm{e}},\ J_2^{\mathrm{e}} := \frac{1}{2}(\ln \boldsymbol{v}^{\mathrm{e}})^{\mathrm{dev}} : (\ln \boldsymbol{v}^{\mathrm{e}})^{\mathrm{dev}},$$

wherein $J^{\mathrm{e}} := \det(\boldsymbol{v}^{\mathrm{e}})$. The stress equation is derived from (A.17) and (A.20):

$$\boldsymbol{\tau}^{\mathrm{x}} = \mathfrak{L}^{\mathrm{e,x}} : \ln \boldsymbol{v}^{\mathrm{e}}, \tag{A.21}$$

where $\mathfrak{L}^{\mathrm{e,x}}$ are the standard fourth order elasticity tensors given by (3), (4), and (8) [73, eqs. (11,12)], [85, Eq. (47)] for all x = a,f,c.

Numerical calculation

In the gauge section of the tensile test specimens, homogeneous deformation and uniaxial stress state prevailed allowing the model calibration and calculations at a single material point. The model was programmed by using the Intel® Fortran application. Under uniaxial loading, only one variable must be solved from the equilibrium equation

$$R_1 := F_{11}^{\mathrm{vep}} - F^{\mathrm{vep}}{}_{\mathrm{n},11} - \Delta t(\bar{D}_{11}^{\mathrm{vep}})F_{11}^{\mathrm{vep}}, \tag{A.22}$$

where the updated state is defined at time $t = t_n + \Delta t$ (Δt is a time increment) and n refers to the known state at t_n. Once the component F_{11}^{vep} is solved ($R_1 \to 0$), $F_{33}^{\mathrm{vep}} = F_{22}^{\mathrm{vep}} = 1/\sqrt{F_{11}^{\mathrm{vep}}}$ ($F_{11}^{\mathrm{vep}}F_{22}^{\mathrm{vep}}F_{33}^{\mathrm{vep}} = 1$) due to virtually incompressible viscoelastic–plastic deformation. The elastic counterpart $\boldsymbol{F}^{\mathrm{e}}$ is available from the decomposition (2) because the total deformation gradient $\boldsymbol{F}$ is available under displacement control (loading, unloading, and stress relaxation). Under creep, however, stress is fixed, and $\boldsymbol{F}^{\mathrm{e}}$ is solved based on the constitutive description

($\boldsymbol{F}^{\mathrm{e}} = \boldsymbol{v}^{\mathrm{e}}$ under uniaxial deformation), $\ln \boldsymbol{v}^{\mathrm{e}} = (\mathfrak{L}^{e,f} + \mathfrak{L}^{e,c} + \mathfrak{L}^{e,a})^{-1}\boldsymbol{\sigma}$. The exponential relationship between $\ln \boldsymbol{v}^{\mathrm{e}}$ and $\boldsymbol{v}^{\mathrm{e}}$ can be solved for component-wise (uniaxial deformation). Finally, the total deformation under creep is solved from the decomposition (2).

Prediction of creep

The compact model formulation and uniaxial loading conditions allow for the development of an explicit expression for creep strain. The creep (and stress relaxation) are long-term processes, preferably with low strain rates (then the rate-dependency term $(\tau/\tau_0)^{1/m}$ in (6) is unity). Denoting $\mathfrak{\gamma} = (\dot{\gamma}^{\mathrm{vep}}/(2\tau) - 1/\eta)^{-1}$ (total viscosity) in (6), $\sigma = \sigma_{11}$, $\dot{\sigma} = \mathrm{d}\sigma/\mathrm{d}t$, and $\dot{\epsilon} = \mathrm{d}/\mathrm{d}t(\ln v_{11}) = \mathrm{d}/\mathrm{d}t(\ln F_{11}) = \mathrm{d}/\mathrm{d}t(\ln v^{\mathrm{e}}_{11} v^{\mathrm{vep}}_{11})$ for uniaxial loads, the constitutive relation

$$\dot{\epsilon} = \frac{\dot{\sigma}}{E} + \frac{\sigma}{\mathfrak{\gamma}} \tag{A.23}$$

holds. Under creep, stress is constant and the time integration results in ($\epsilon = \sigma_0/E$ as $t = 0$)

$$\epsilon = \sigma_0\left(\frac{1}{E} + \frac{t}{\mathfrak{\gamma}}\right). \tag{A.24}$$

It was found that $s^{\mathrm{a}} \gg \varsigma I_1/3$ in (7) for $\dot{\gamma}^{\mathrm{vep}}$ when (A.24) can be approximated as

$$\epsilon = \sigma_0\left(\frac{1}{E} + t\left(\frac{\dot{\gamma}^{\mathrm{a}}_0 \tau_0^{1/m-1}}{(s^{\mathrm{a}})^{1/m}} - \frac{1}{\eta}\right)\right), \tag{A.25}$$

where $\tau_0 = \tau(t = 0)$. According to (A.25), creep strain increases rapidly with stress ($m \sim 0.1$) and is suppressed when $1/\mathfrak{\gamma} \sim \dot{\gamma}^{\mathrm{a}}_0 \tau_0^{1/m-1}/(s^{\mathrm{a}})^{1/m} - 1/\eta \to 0$ (it is required that the term $1/\mathfrak{\gamma}$ is positive or zero; otherwise, viscoplastic deformation does not develop). Although the model provides a linear relationship between creep strain and time, creep violation remains small at the relatively small stress levels present in practice.

Prediction of stress relaxation

When the strain is regarded as fixed, Eq. (A.23) is equal to zero and

$$\frac{\mathrm{d}\sigma}{\sigma} = -\frac{E}{\mathfrak{\gamma}}\mathrm{d}t = -E(\dot{\gamma}^{\mathrm{a}}_0 \frac{(2/\sqrt{3}\sigma)^{1/m-1}}{(s^{\mathrm{a}} - 1/3\varsigma\sigma)^{1/m}} - \frac{1}{\eta})\mathrm{d}t. \tag{A.26}$$

Noting $s^{\mathrm{a}} \gg \varsigma I_1/3$, the integration of (A.26) yields ($\sigma = \sigma_0$ as $t = 0$)

$$\sigma = \sigma_0 \exp\left(-E(\dot{\gamma}^{\mathrm{a}}_0 \frac{(2/\sqrt{3})^{1/m-1}}{(s^{\mathrm{a}})^{1/m}} m(\sigma^{1/m} - \sigma_0^{1/m}) - \frac{t}{\eta})\right). \tag{A.27}$$

In other words, the reduction in the stress is exponential which is in agreement with the experimental observations. Moreover, Eq. (A.26) reveals that $\mathrm{d}\sigma \to 0$ as $\mathfrak{\gamma} \to \infty$ ($t \to \infty$) and, consequently, $\sigma \to \bar{\sigma}$, that is, the stress is not relaxed to zero, but asymptotically approaches the limit $\bar{\sigma} > 0$. This is a characteristic of viscous (composite) materials [77,78,86].

Data availability

Source data supporting the findings of this study are available upon request. We provide the source data underlying Table 3.

References

[1] A. Bourmaud, J. Beaugrand, D. Shah, V. Placet, C. Baley, Towards the design of high-performance plant fibre composites, Prog. Mater. Sci. 97 (2018) 347–408.

[2] C. Zhang, J. Xue, X. Yang, Y. Ke, R. Ou, Y. Wang, S.A. Madbouly, Q. Wang, From plant phenols to novel bio-based polymers, Prog. Polym. Sci. 125 (2022) 101473.

[3] P. Zarrintaj, F. Seidi, M.Y. Azarfam, M.K. Yazdi, A. Erfani, Biopolymer-based composites for tissue engineering applications: A basis for future opportunities, Compos. B Eng. 258 (2023) 110701.

[4] N. Ning, S. Fu, W. Zhang, F. Chen, K. Wang, H. Deng, Q. Zhang, Q. Fu, Realizing the enhancement of interfacial interaction in semicrystalline polymer/filler composites via interfacial crystallization, Prog. Polym. Sci. 37 (2012) 1425–1455.

[5] L. Qi, W. Tian, J. Zhou, Numerical evaluation of effective elastic properties of composites reinforced by spatially randomly distributed short fibers with certain aspect ratio, Compos. Struct. 131 (2015) 843–851.

[6] Z. Zhang, H. Zhu, R. Yuan, S. Wang, T. Fan, Y. Rezgui, D. Zhang, The near-isotropic elastic properties of interpenetrating composites reinforced by regular fibre-networks, Mater. Des. 221 (2022) 110923.

[7] Y. Cai, H. Sun, Thermo-viscoelastic analysis of three-dimensionally braided composites, Compos. Struct. 98 (2013) 47–52.

[8] B. Fallqvist, M. Kroon, Constitutive modelling of composite biopolymer networks, J. Theoret. Biol. 395 (2016) 51–61.

[9] C. Naili, I. Doghri, T. Kanit, M. Sukiman, A. Aissa-Berraies, A. Imad, Short fiber reinforced composites: Unbiased full-field evaluation of various homogenization methods in elasticity, Compos. Sci. Technol. 187 (2020) 107942.

[10] H. Chandekar, V.V. Chaudhari, S. Waigaonkar, Theoretical models for stiffness prediction of short fibre composites, in: Materials Today: Proceedings 57, Part 2, 2022, pp. 711–714.

[11] X. Wang, H. Zhu, B. Song, X. Chen, D. Kennedy, Y. Shi, Nonlinear elastic behaviors and deformation mechanisms of nano-structured crosslinked biopolymer networks, Extrem. Mech. Lett. 61 (2023) 102017.

[12] J. Andersons, J. Modniks, R. Joffe, B. Madsen, K. Nättinen, Apparent interfacial shear strength of short-flax-fiber/starch acetate composites, Int. J. Adhes. Adhes 64 (2016) 78–85.

[13] J. Modniks, J. Andersons, Modeling the non-linear deformation of a short-flax-fiber-reinforced polymer composite by orientation averaging, Compos.: Part B 54 (2013) 188–193.

[14] D. Notta-Cuvier, F. Lauro, B. Bennani, R. Balieu, An efficient modelling of inelastic composites with misaligned short fibres, Int. J. Solids Struct. 50 (2013) 2857–2871.

[15] B. Miled, S. Kammoun, I. Belyamani, L. Cauret, Manufacturing, characterization, and macromechanical modeling of short flax/hemp fiber-hybrid reinforced polypropylene, Forces Mech. 15 (2024) 100269.

[16] P.A. Hessman, F. Welschinger, K. Hornberger, T. Böhlke, On mean field homogenization schemes for short fiber reinforced composites: Unified formulation, application and benchmark, Int. J. Solids Struct. (2021) 230–231, 111141.

[17] A.P. Dey, F. Welschinger, M. Schneider, S. Gajek, T. Böhlke, Rapid inverse calibration of a multiscale model for the viscoplastic and creep behavior of short fiber-reinforced thermoplastics based on deep material networks, Int. J. Plast. 160 (2023) 103484.

[18] F. Praud, K. Schneider, G. Chatzigeorgiou, F. Meraghni, Microstructure generation and full-field multi-scale analyses for short fiber reinforced thermoplastics: Application to PA66GF composites, Compos. Struct. 341 (2024) 118175.

[19] D. Jeulin, S. Forest, Statistical approach to the representative volume element size of random composites, in: Digital Materials: Continuum Numerical Methods At the Mesoscopic Scale, John Wiley & Sons, 2024.

[20] M. Schneider, The sequential addition and migration method to generate representative volume elements for the homogenization of short fiber reinforced plastics, Comput. Mech. 59 (2017) 247–263.

[21] J.A.W. van Dommelena, D.M. Parks, M.C. Boyce, W.A.M. Brekelmans, F.P.T. Baaijens, Micromechanical modeling of the elasto-viscoplastic behavior of semi-crystalline polymers, J. Mech. Phys. Solids 51 (2003) 519–541.

[22] S. Venkatesan, S. Basu, Investigations into crazing in glassy amorphous polymers through molecular dynamics simulations, J. Mech. Phys. Solids 77 (2015) 123–145.

[23] T. Barriere, X. Gabrion, S. Holopainen, J. Jokinen, Testing and analysis of solid polymers under large monotonic and long-term cyclic deformation, Int. J. Plast. 135 (2020) 102781.

[24] T. Barriere, A. Cherouat, X. Gabrion, S. Holopainen, Short- to long-term deformation behavior, failure, and service life of amorphous polymers under cyclic torsional and multiaxial loadings, Int. J. Plast. 147 (2021) 103106.

[25] Z. Yang, Y. Yabansu, R. Al-Bahrani, W. Liao, A. Choudhary, S. Kalidindi, A. Agrawal, Deep learning approaches for mining structure–property linkages in high contrast composites from simulation datasets, Comput. Mater. Sci. 151 (2018) 278–287.

[26] C. Zhai, T. Shi, J. Yeo, Discovery and design of soft polymeric bio-in-spired materials with multiscale simulations and artficial intelligence, J. Mater Chem. B 8 (2020) 6562–6587.

[27] B.G. Laycock, C.M. Chan, P.J. Halley, A review of computational approaches used in the modelling, design, and manufacturing of biodegradable and biobased polymers, Prog. Polym. Sci. 157 (2024) 101874.

[28] S. Lu, X. Zhang, Y. Hu, J. Chu, Q. Kan, G. Kang, Machine learning-based constitutive parameter identification for crystal plasticity models, Mech. Mater. 203 (2025) 105283.

[29] D.T. Fullwood, B.L. Adams, S.R. Kalidindi, A strong contrast homogenization formulation for multi-phase anisotropic materials, J. Mech. Phys. Solids 56 (2008) 2287–2297.

[30] A. Tavassoli, Y. Waghei, A. Nazemi, Comparison of Kriging and artificial neural network models for the prediction of spatial data, J. Stat. Comput. Simul. 92 (2021) 352–369.
[31] S. Ling, Z. Wu, J. Mei, S. Lv, An efficient machine learning-based model for predicting the stress–strain relationships of thermoplastic polymers with limited testing data, Compos. B: Eng. 283 (2024) 111600.
[32] S. Gajek, M. Schneider, T. Böhlke, On the micromechanics of deep material networks, J. Mech. Phys. Solids 142 (2020) 103984.
[33] A.J. Thomas, E. Barocio, A machine learning approach to determine the elastic properties of printed fiber-reinforced polymers, Compos. Sci. Technol. 220 (2022) 109293.
[34] S. Holopainen, O. Kuusi, Big data tulee - nykytila ja tulevaisuuden mahdollisuudet (mainly in finnish), Futura 2 (113) (2016).
[35] C. Liu, B. Chamberlain, E. McCoy, What is the value of experimentation and measurement, Data Sci. Eng. 5 (2020) 152–167.
[36] K.J. Jem, B. Tan, The development and challenges of poly (lactic acid) and poly (glycolic acid), Adv. Ind. Eng. Polym. Res. 3 (2020) 60–70.
[37] R.A. Ilyas, S.M. Sapuan, M.M. Harussani, M.Y.A.Y. Hakimi, M.Z.M. Haziq, M.S.N. Atikah, M.R.M. Asyraf, M.R. Ishak, M.R. Razman, N.M. Nurazzi, M.N.F. Norrrahim, H. Abral, M. Asrofi, Polylactic acid (PLA) biocomposite: Processing, additive manufacturing and advanced applications, Polymers 13 (2021) 13081326.
[38] A. Nazir, O. Gokcekaya, K.M.M. Billah, O. Ertugrul, J. Jiang, J. Sun, S. Hussain, Multi-material additive manufacturing: A systematic review of design, properties, applications, challenges, and 3D printing of materials and cellular metamaterials, Mater. Des. 226 (2023) 111661.
[39] R. Scaffaro, M.C. Citarrella, A. Catania, L. Settanni, Green composites based on biodegradable polymers and anchovy (Engraulis Encrasicolus) waste suitable for 3D printing applications, Compos. Sci. Technol. 230 (2022) 109768.
[40] F. ACT4504MR, Market research survey, in: 10 Years Historical Data, Analysis and Forecast, Technical Report, FACT.MR, 2022.
[41] R. Hu, J.K. Lim, Fabrication and mechanical properties of completely biodegradable hemp fiber reinforced polylactic acid composites, J. Compos. Mater. 41 (2007) 1655–1669.
[42] M.A. Sawpan, K.L. Pickering, A. Fernyhough, Effect of fibre treatments on interfacial shear strength of hemp fibre reinforced polylactide and unsaturated polyester composites, Compos. Part A Appl. Sci. Manuf. 42 (2011) 1189–1196.
[43] B. Baghaei, M. Skrifvars, M. Rissanen, S. Ramamoorthy, Mechanical and thermal characterization of compression moulded polylactic acid natural fiber composites reinforced with hemp and lyocell fibers, J. Appl. Polym. Sci. 131 (40534) (2014).
[44] S. Morin, L. Dumoulin, et al., Green composites based on thermoplastic starches and various natural plant fibers: Impacting parameters of the mechanical properties using machine-learning, Polym. Compos. 42 (2021) 3458–3467.
[45] A. Rosa-Sainz, G. Centeno, M.B. Silva, J.A. López-Fernández, A.J. Martínez-Donaire, C. Vallellano, On the determination of forming limits in polycarbonate sheets, Materials 13 (928) (2020).
[46] A.K. Trivedi, M.K. Gupta, H. Singh, PLA based biocomposites for sustainable products: A review, Adv. Ind. Eng. Polym. Res. 6 (2023) 382–395.
[47] B. Skuratowicz, Mechanical Properties of Hemp Fiber Reinforced Polylactic Acid Composites (Ph.D. thesis), Oregon State University, United States, 2023.
[48] C.G. Skamniotis, M. Elliott, M.N. Charalambides, On modelling the constitutive and damage behaviour of highly non-linear bio-composites - mesh sensitivity of the viscoplastic damage law computations, Int. J. Plast. 114 (2019) 40–62.
[49] A.L. Duigou, D. Correa, M. Ueda, R. Matsuzaki, M. Castrog, A review of 3D and 4D printing of natural fibre biocomposites, Mater. Des. 194 (2020) 108911.
[50] J. Proy, F. Massa, D. Notta-Cuvier, F. Lauro, T. Tison, G. Spingler, Integrating fibers and injection molding process variability in short-natural-fiber-reinforced thermoplastics behavior: A review, Mater. Today Commun. 29 (2021) 102785.
[51] T. Belytschko, W.K. Liu, B. Moran, Nonlinear Finite Elements for Continua and Structures, John Wiley & Sons, Chichester, 2000.
[52] S. Mortazavian, A. Fatemi, Effects of fiber orientation and anisotropy on tensile strength and elastic modulus of short fiber reinforced polymer composites, Compos.: Part B 72 (2015) 116–129.
[53] T. Barriere, X. Gabrion, S. Holopainen, A compact constitutive model to describe the viscoelastic–plastic behaviour of glassy polymers: Comparison with monotonic and cyclic experiments and state-of-the-art models, Int. J. Plast. 122 (2019) 31–48.
[54] Z. Bartczak, Deformation of semicrystalline polymers - the contribution of crystalline and amorphous phases, Polimery 11 (2017) 785–912.
[55] S. Corneilliea, M. Smet, PLA architectures: the role of branching, Polym. Chem. 6 (2015) 850–867.
[56] S. Holopainen, T. Barriere, Modeling of mechanical behavior of amorphous solids undergoing fatigue loadings, with application to polymers, Comput. Struct. 199 (2018) 57–73.
[57] V. Placet, F. Trivaudey, O. Cisse, V. Gucheret-Retel, M.L. Boubakar, Diameter dependence of the apparent tensile modulus of hemp fibres: A morphological, structural or ultrastructural effect? Compos.: Part A 43 (2012) 275–287.
[58] E.M. Arruda, M.C. Boyce, Experimental and analytical investigation of the large strain compressive and tensile response of glassy polymers, Polym. Eng. Sci. 30 (1990) 1288–1298.
[59] L. Anand, N.M. Ames, On modeling the micro-indentation response of an amorphous polymer, Int. J. Plast. 22 (2006) 1123–1170.
[60] A. Amiri-Rad, L.V. Pastukhov, L.E. Govaert, J.A.W. van Dommelen, An anisotropic viscoelastic-viscoplastic model for short-fiber composites, Mech. Mater. 137 (2019) 103141.
[61] A.S. Argon, A theory for the low-temperature plastic deformation of glassy polymers, Phil. Mag. 28 (1973) 839–865.
[62] S. Holopainen, Modeling of the mechanical behavior of amorphous glassy polymers under variable loadings and comparison with state-of-the-art model predictions, Mech. Mater. 66 (2013) 35–58.
[63] B.B. Lynch, The Crystallization Kinetics of Polylactic Acid (Pla)Processed Through Solid-State/Melt Extrusion, Bucknell University, United States, 2014.
[64] T. Barrière, S. Carbillet, X. Gabrion, S. Holopainen, Prediction of short- to long-term cyclic deformation behavior and fatigue life of polymers, Polymers 16 (1640) (2024).
[65] N.F.M. Rawi, K. Jayaraman, D. Bhattacharyya, A performance study on composites made from bamboo fabric and poly(lactic acid), J. Reinf. Plast. Compos. 32 (2013) 1513–1525.
[66] M. Iguchi, Y. Hiraga, K. Kasuya, T.M. Aida, M. Watanabe, Y. Sato, Jr., R.L.S, Viscosity and density of poly(ethylene glycol) and its solution with carbon dioxide at 353.2K and 373.2K at pressures up to 15 mpa, J. Supercrit. Fluids 97 (2015) 63–73.
[67] R. Fangueiro, S. Rana, Advances in Natural Fibre Composites, Springer, 2018, pp. 1–25.
[68] V. Mazzanti, M.S. de Luna, R. Pariante, F. Mollica, G. Filippone, Natural fiber-induced degradation in PLA-hemp biocomposites in the molten state, Compos. Part A 137 (2020) 105990.
[69] Q. Fang, M.A. Hanna, Rheological properties of amorphous and semicrystalline polylactic acid polymers, Ind. Crop. Prod. 10 (1999) 47–53.
[70] C. Zhang, W. Liu, S. Ma, B. Wang, G. Wu, J. Cheng, Z. Ni, G. Zhao, Strength and toughness of semicrystalline polymer fibers: Influence of molecular chain entanglement, Polymer 304 (2024) 127119.
[71] M.A. Sawpan, K.L. Pickering, A. Fernyhough, Improvement of mechanical performance of industrial hemp fibre reinforced polylactide biocomposites, Compos. Part A Appl. Sci. Manuf. 42 (2011) 310–319.
[72] C. Dreistadt, A.S. Bonnet, P. Chevrier, P. Lipinski, Experimental study of the polycarbonate behaviour during complex loadings and comparison with the boyce, parks and argon model predictions, Mater. Des. 30 (2009) 3126–3140.
[73] S. Holopainen, M. Wallin, Modeling of long-term behavior of amorphous glassy polymers, ASME J. Eng. Mater. Tech. 135 (2012) 1–11.
[74] B. Rhoads, Analysis of Hemp Fiber Reinforced Polylactide Composite under High Strain-Rate (Ph.D. thesis), University of Mississippi, US, 2022.
[75] J. Luo, Q. Luo, G. Zhang, Q. Li, G. Sun, On strain rate and temperature dependent mechanical properties and constitutive models for additively manufactured polylactic acid (PLA) materials, Thin-Walled Struct. 179 (2022) 109624.
[76] M. Durante, A. Formisano, L. Boccarusso, A. Langella, L. Carrino, Creep behaviour of polylactic acid reinforced by woven hemp fabric, Compos. Part B 124 (2017) 16–22.
[77] C. Martins, V. Pinto, R.M. Guedes, A.T. Marques, Creep and stress relaxation behaviour of PLA-PCL fibres - A linear modelling approach, Procedia Eng. 114 (2015) 768–775.
[78] K. Tüfekci, B.G. Çakan, V.M. Küçükakarsu, Stress relaxation of 3D printed PLA of various infill orientations under tensile and bending loadings, J. Appl. Polym. Sci. 140 (2023) 1–10.
[79] M. Noghabaei, Y. Liu, K. Han, Automated compatibility checking of prefabricated components using 3D as-built models and BIM, Autom. Constr. 143 (2022) 104566.
[80] R. Jose, S. Ramakrishna, Materials 4.0: materials big data enabled materials discovery, Appl. Mater Today 10 (2018) 127–132.
[81] F. Pedregosa, et al., Machine learning in python, J. Mach. Learn. Res. 12 (2011) 2825–2830.
[82] P. Rivas-Perea, J. Cota-Ruiz, D.G. Chaparro, J.A.P. Venzor, A.Q. Carreon, J.G. Rosiles, Support vector machines for regression: A succinct review of large-scale and linear programming formulations, Int. J. Intell. Sci. 3 (2013) 5–14.
[83] R. Fan, P. Chen, C. Lin, Working set selection using second order information for training support vector machines, J. Mach. Learn. Res. 6 (2005) 1871–1918.
[84] J.L. Chaboche, Thermodynamic formulation of constitutive equations and application to the viscoplasticity and viscoelasticity of metals and polymers, Int. J. Solids Struct. 34 (1997) 2239–2254.
[85] S. Holopainen, T. Barriere, G. Cheng, R. Kouhia, Continuum approach for modeling fatigue in amorphous glassy polymers. applications to the investigation of damage-ratcheting interaction in polycarbonate, Int. J. Plast. 91 (2017) 109–133.
[86] M. Al-Haika, M.R. Vaghara, H. Garmestani, M. Shahawy, Viscoplastic analysis of structural polymer composites using stress relaxation and creep data, Compos.: Part B 32 (2001) 165–170.